Chemical Abundances of H II Regions in the Starburst Galaxy NGC 1705[†]

Henry Lee and Evan D. Skillman

Department of Astronomy, University of Minnesota, 116 Church St. SE, Minneapolis, MN 55455 USA hlee@astro.umn.edu, skillman@astro.umn.edu

ABSTRACT

We report optical spectroscopy of 16 H II regions in NGC 1705 and [O III] λ 4363 detections for the first time in five H II regions. The resulting mean oxygen abundance derived directly from measured electron temperatures is $12 + \log(O/H) = 8.21 \pm 0.05$, which corresponds to [O/H] = -0.45, or 35% of the solar value. There are no significant spatial inhomogeneities in [O III] \(\lambda \) 4363 oxygen abundances from H II regions at a radius approximately 10" from the super star cluster. In H II regions where [O III] λ 4363 was not measured, oxygen abundances derived with bright-line methods (accurate only to 0.2 dex) are in agreement with direct values of the oxygen abundance. Faint narrow He II λ 4686 emission is found in two H II regions, but the implied contribution from O^{+3} to the total oxygen abundance is only 0.01 dex. The mean argon-, neon, and nitrogen-to-oxygen abundance ratios are consistent with mean values for other dwarf irregulars, blue compact dwarf galaxies, and H II galaxies at comparable oxygen abundances. Interestingly, the nitrogen-to-oxygen abundance ratio in the ionized H II gas agrees with the value for the neutral HI, even though the metallicity of the neutral gas may be a factor of six lower than that of the ionized gas. This may be indicative of low-metallicity gas in the halo of the galaxy. Extinction values, A_V , derived from observed Balmer line ratios along lines of sight to H II regions are in the range between zero and 0.9 mag. Significant and variable extinction may have important effects on the interpretation of resolved stellar populations and derived star formation histories. With respect to the metallicity-luminosity and metallicity-gas fraction diagnostics, the measured oxygen abundance for NGC 1705 is comparable to Local Group dwarf irregulars at a given luminosity and gas fraction. Simple chemical evolution models suggest that the galaxy is quickly evolving into a gas-poor dwarf galaxy.

Subject headings: galaxies: abundances — galaxies: evolution — galaxies: individual (NGC 1705) — galaxies: irregular — galaxies: starburst

[†] Based on EFOSC2 observations collected at the European Southern Observatory, Chile.

1. Introduction

Dwarf galaxies play a key role in our understanding of galaxy formation and evolution, star formation, and cosmology. These are thought to be the primary building blocks in hierarchical models of structure formation (e.g., Kauffmann et al. 1993). Dwarf galaxies have low masses and, typically, low metallicities (below half-solar; e.g., Mateo 1998). However, there is a range of morphologies, and recent attention has been paid to understanding the relationships between different types of dwarf galaxies and/or whether or not they all have a common progenitor. Dwarf irregular galaxies could be spending most of their lives in a relatively quiescent phase by forming stars at a low constant rate (e.g., IC 1613, Skillman et al. 2003c). However, blue compact dwarf galaxies appear to host recent bursts of star formation, whose optical luminosities are often larger than the underlying stellar populations. Blue compact dwarfs then may be related to gas-poor dwarf spheroidal galaxies, if the latter experienced in the past strong burst(s) of star formation, which eventually blew out their gas content. Because of their low gravitational potentials, dwarf galaxies are expected to lose gas and metals in supernova-driven winds or outflows. These winds may be an important mechanism to the chemical enrichment of the intergalactic medium (e.g., Garnett 2002).

Starbursts offer a unique glimpse into a distinct phase in the life of a dwarf galaxy, clues to the possible evolutionary relationship between different types of dwarf galaxies, and insights into the processes regarding the formation of massive stars. In galaxies with strong starbursts, star formation occurs at a rate much larger than the past average rate. The physical conditions within starburst regions are thought to be similar to conditions in the early universe, where the first generations of stars formed and galaxy assembly occurred. Recent ultraviolet studies, e.g., with the Far Ultraviolet Spectroscopic Explorer (FUSE), have recently revolutionized the field, because the ultraviolet probes directly the hot and massive star content in the starbursts. Optical emission-line spectra of H II regions are dominated by strong narrow emission lines, a relatively weak continuum which rises towards blue wavelengths, and weak absorption Balmer-line features. These spectra provide diagnostics on the conditions within the ionized nebular gas, information about the total reddening along various lines of sight, and information about the most recent chemical enrichment in the form of elemental abundances and ratios (e.g., Kewley & Dopita 2002). In fact, the metallicity may be the most important parameter in determining the properties of starburst galaxies at ultraviolet wavelengths (e.g., Heckman et al. 1998; Tremonti et al. 2001).

1.1. NGC 1705

NGC 1705 is a nearby, isolated, amorphous or blue compact dwarf galaxy, which has been the subject of much recent attention in the literature. A basic list of properties is given in Table 1. Near the center is a 10^5 M_{\odot} super star cluster (SSC), also known as NGC 1705-1 (Melnick et al. 1985; Meurer et al. 1989, 1992), whose properties appear to be similar to Galactic globular clusters

(Ho & Filippenko 1996). However, the SSC is not situated exactly at the center of the galaxy (Tosi et al. 2001), which was previously suggested by Heckman & Leitherer (1997) and Hensler et al. (1998). Tosi et al. (2001) showed that stars more massive than about 30 M_☉ and younger than 20 Myr were located within 4" of the SSC. The most recent episode of star formation appears to have been dominated by the SSC, whose age has been measured to be in the range 10 to 15 Myr (Melnick et al. 1985; O'Connell et al. 1994; Heckman & Leitherer 1997; Vázquez et al. 2004). The SSC is surrounded by clusters of young massive stars, which are seen as bright H II regions (Fig. 1; e.g., Melnick et al. 1985; Meurer et al. 1989, 1992; Hunter et al. 1993; Marlowe et al. 1995; Gil de Paz et al. 2003). The underlying stellar population has been shown to be a composite mix of stars ranging in age from 0.1 to 10 Gyr (Meurer et al. 1992; Quillen et al. 1995; Annibali et al. 2003). Greve et al. (1996) detected no CO emission at the position of the SSC. Using FUSE to look for far-ultraviolet absorption lines of H_2 , Hoopes et al. (2004) measured the central 30" by 30" in NGC 1705 and set an upper limit of 3.90 × 10¹⁴ cm⁻² for the total H_2 column density.

NGC 1705 is thought to be a prototype for dwarf galaxies presently undergoing mass loss or outflows. Evidence from previous work is summarized here in chronological order. Lamb et al. (1985) observed the galaxy with the International Ultraviolet Explorer (IUE), and noted that the galaxy was going through an overall modest enhancement of star formation, which was superposed on the center undergoing a post-starburst phase. York et al. (1990) also used IUE data and proposed that absorption lines seen in their ultraviolet spectra (e.g., Al II λ 1671 Å) arose from intervening absorption systems in the interstellar medium of the galaxy. Meurer et al. (1992) published a comprehensive study combining imaging and spectroscopy from ultraviolet to radio wavelengths. A complex set of arc and loop features seen in $H\alpha$ roughly centered on the SSC suggested that explosive events had clearly occurred in the system, and that the SSC was responsible for creating a very large, bright, central "superbubble" of ionized gas. They also showed that line profiles in $H\alpha$ exhibited multiple components with radial velocity differences of about 100 km s⁻¹ across the center of the galaxy. The largest blueshifted component corresponded to a strong interstellar absorption feature, which suggested that this component or feature was expanding and situated in front of the SSC. Hunter et al. (1993) also confirmed the existence of large $H\alpha$ filaments centered on the SSC. With Fabry-Perot and echelle spectroscopic data, Marlowe et al. (1995) showed from $H\alpha$ kinematics and profiles that the superbubble was expanding and that the dynamical timescale was of order 10 Myr. Among amorphous galaxies, Marlowe et al. (1997) classified NGC 1705 as a galaxy with "a strong core and explosive H α morphology." With ROSAT, Hensler et al. (1998) found embedded among the $H\alpha$ arcs two regions of soft X-ray emission. These structures suggested that the X-ray pockets were surrounded by cool gas shells in $H\alpha$ emission, and that these features could be interpreted as being the outer plumes of the same superbubble. Using Goddard High-Resolution Spectrograph (GHRS) archival data from the Hubble Space Telescope (HST), Sahu &

¹With *HST* narrow-band imaging of four starburst galaxies, Calzetti et al. (2004) showed that the central starbursts produce sufficient mechanical energy from shocks arising from massive star winds and supernova explosions to explain the nonphotoionized gas content and that the nonphotoionized gas is associated with extended shells or filaments.

Blades (1997) and Sahu (1998) reported three absorption-line systems from ultraviolet absorption lines. One of the systems with the largest line-of-sight velocity was associated with a blueshifted emission component of the expanding supershell. The absorption system contained strong Si II and Al II absorption, but weak Fe II λ 1608 absorption. Heckman et al. (2001) measured O VI outflow with FUSE, and suggested that the warm and hot gas phases were flowing out of the galaxy. Johnson et al. (2003) did not detect any thermal radio sources within NGC 1705, which supported the idea that the galaxy is currently in a post-starburst phase. This would mean that at the present time, any massive star formation has somehow been completely shut off in the galaxy, even though a strong starburst event occurred ≈ 10 Myr ago.

The SSC has likely been the source responsible for expelling the outflowing gas in the last ≈ 10 Myr (e.g., O'Connell et al. 1994; Suchkov et al. 1994; Heckman & Leitherer 1997; Tosi et al. 2001). Naturally, the SSC was also thought to be the main source of ionization in the galaxy. However, Vázquez et al. (2004) showed that the SSC could not be the dominant ionizing source in the galaxy; instead, O-type stars within H II regions surrounding the SSC are more likely to be the sources of the ionizing radiation.

For the metallicities typical of dwarf galaxies, oxygen is a relatively abundant element, and regulates physical conditions as the primary coolant within H II regions (e.g., Dinerstein 1990; Skillman 1998). The cooling is accomplished primarily through the optical emission lines of oxygen. Oxygen abundances from H II regions can help constrain the modeling required to extract the metallicity in the hot, ejected, X-ray emitting gas, which is expected to appear in galaxy halos (e.g., Martin et al. 2002). The nebular oxygen abundance for NGC 1705 was thought to be comparable to that of the LMC (12+log(O/H) = 8.35; Russell & Dopita 1992). However, previous determinations of oxygen abundances have been derived in the absence of measurements for the temperature-sensitive [O III] λ 4363 emission line (Lamb et al. 1985; Meurer et al. 1992; Storchi-Bergmann et al. 1994; Heckman et al. 1998). Oxygen abundances derived using bright-line or empirical methods are accurate to within 0.2 dex (§ 4.2; also Lee et al. 2003a; Skillman et al. 2003b). As part of an ongoing program to understand the nature of nearby starburst galaxies, we acquired spectra of H II regions in NGC 1705 in order to detect the [O III] λ 4363 line, to derive subsequently electron temperatures and direct oxygen abundances, and to measure extinction values using Balmer line ratios along different lines of sight.

The paper is organized as follows. Observations and reductions of the data are presented in \S 2, the measurements are given in \S 3, derivations of chemical abundances are described in \S 4, discussion of the results is presented in \S 5, and the conclusions are given in \S 6. For the remainder of this paper, we adopt $12 + \log(O/H) = 8.66$ as the revised solar value for the oxygen abundance, and $Z_{\odot} = 0.0126$ as the revised solar mass fraction in the form of metals (Asplund et al. 2004).

2. Observations and Reductions

Long-slit spectroscopic observations were carried out during new moon on 2003 Aug. 27, 28, and 30 UT with the ESO Faint Object Spectrograph and Camera (EFOSC2) instrument on the 3.6-m telescope at ESO La Silla Observatory. Conditions were mostly cloudy on Aug. 30, and the data obtained were not used. Details of the instrumentation employed and the log of observations are listed in Tables 2 and 3, respectively. The H α images published by Gil de Paz et al. (2003) were used to optimize slit placements on the galaxy. Two-minute H α acquisition images were obtained in order to set the best position angle of the slit, so that the slit could go through as many H II regions possible. Data were obtained with three slit placements; the position angles are listed in Table 3. Actual slit orientations on the galaxy are shown in Figs. 1 to 4 inclusive. H II regions for which spectra were acquired are given in Table 4. The locations of H II regions were compared and matched with identifications in the images published by Melnick et al. (1985) and Meurer et al. (1992).

The spectra were reduced using standard IRAF² routines. Data obtained on a given night were reduced independently. The raw two-dimensional images were subtracted for bias and trimmed. Dome flat exposures were used to remove pixel-to-pixel variations in response, and twilight flats were acquired at dusk each night to correct for variations over larger spatial scales. To correct for the "slit function" in the spatial direction, the variation of illumination along the slit was taken into account using dome and twilight flats. Cosmic rays were removed in the addition of multiple exposures. For the single frames taken with slits B and C, the spectra were inspected visually for cosmic rays. Wavelength calibration was obtained using helium-argon (He-Ar) arc lamp exposures taken throughout each night. With the 5" slit, exposures of standard stars Feige 110, G138–31, LTT 1788, LTT 7379, and LTT 9491 were used for flux calibration. The flux accuracy is listed in Table 3. One-dimensional spectra for each H II region were obtained with unweighted summed extractions. Spectra for which $[O III]\lambda$ 4363 was detected are shown in Fig. 5. For completeness, the spectrum of the SSC with slit C is shown in Fig. 6. We observed weak $[O III]\lambda$ 5007 and $H\alpha$, as seen previously by Melnick et al. (1985). The spectrum of the SSC is not discussed further in the remainder of this paper.

3. Measurements

Emission-line strengths were measured using software developed by M. L. McCall and L. Mundy; see Lee (2001); Lee et al. (2003b,c). Because the systemic velocity for NGC 1705 is over 600 km s⁻¹, there is sufficient wavelength offset from the Hg I λ 4358 sky line for the [O III] λ 4363 emission line to be detected. The spectra clearly indicate the presence of [O III] λ 4363 in five H II

²IRAF is distributed by the National Optical Astronomical Observatories, which is operated by the Associated Universities for Research in Astronomy, Inc., under contract to the National Science Foundation.

regions: A3, B3, B4, B6, and C6.

Corrections for reddening and for underlying absorption and abundance analyses were performed with SNAP (Spreadsheet Nebular Analysis Package, Krawchuk et al. 1997). Balmer fluxes were first corrected for underlying Balmer absorption with an equivalent width 2 Å (McCall et al. 1985; Lee et al. 2003c). Here, the uncertainty in the correction for underlying Balmer absorption was assumed to be zero (but see also the discussion below). H α and H β fluxes were used to derive reddening values, E(B-V), using the equation

$$\log \frac{I(\lambda)}{I(H\beta)} = \log \frac{F(\lambda)}{F(H\beta)} + 0.4 E(B - V) [A_1(\lambda) - A_1(H\beta)]$$
 (1)

(Lee et al. 2003b). F and I are the observed flux and corrected intensity ratios, respectively. Intrinsic case-B Balmer line ratios determined by Storey & Hummer (1995) were assumed. $A_1(\lambda)$ is the extinction in magnitudes for E(B-V)=1, i.e., $A_1(\lambda)=A(\lambda)/E(B-V)$, where $A(\lambda)$ is the monochromatic extinction in magnitudes. Values of A_1 were obtained from the Cardelli et al. (1989) reddening law as defined by a ratio of the total to selective extinction, $R_V = A_V/E(B-V) = 3.07$, which in the limit of zero reddening is the value for an A0V star (e.g., Vega) with intrinsic color $(B-V)^0=0$. Because [S II] $\lambda\lambda$ 6716,6731 lines were generally unresolved, $n_e=100$ cm⁻³ was adopted for the electron density. Errors in the derived E(B-V) were computed from the maximum and minimum values of the reddening based upon 2σ errors in the fits to emission lines.

Observed flux (F) and corrected intensity (I) ratios are listed in Tables 5a to 5c inclusive. The listed errors for the observed flux ratios at each wavelength λ account for the errors in the fits to the line profiles, their surrounding continua, and the relative error in the sensitivity function stated in Table 3. Errors in the corrected intensity ratios account for maximum and minimum errors in the flux of the specified line and of the H β reference line. At the H β reference line, errors for both observed and corrected ratios do not include the error in the flux. Also given for each H II region are: the observed H β flux, the equivalent width of the H β line in emission, and the derived reddening from SNAP.

Where $[O III]\lambda$ 4363 is measured, we also have performed the additional computations to check the consistency of our results. Equation (1) can be generalized and rewritten as

$$\log \frac{I(\lambda)}{I(H\beta)} = \log \frac{F(\lambda)}{F(H\beta)} + c(H\beta) f(\lambda), \tag{2}$$

where $c(H\beta)$ is the logarithmic extinction at H β , and $f(\lambda)$ is the wavelength-dependent reddening function (Aller 1984; Osterbrock 1989). From Equations (1) and (2), we obtain

$$c(H\beta) = 1.43 E(B - V) = 0.47 A_V.$$
 (3)

The reddening function normalized to H β is derived from the Cardelli et al. (1989) reddening law, assuming $R_V = 3.07$. As described in Skillman et al. (2003b), values of $c(H\beta)$ were derived from the error weighted average of values for $F(H\alpha)/F(H\beta)$, $F(H\gamma)/F(H\beta)$, and $F(H\delta)/F(H\beta)$ ratios

while simultaneously solving for the effects of underlying Balmer absorption with equivalent width, EW_{abs}. We assumed that EW_{abs} was the same for H α , H β , H γ , and H δ . Uncertainties in $c(H\beta)$ and EW_{abs} were determined from Monte Carlo simulations (Olive & Skillman 2001; Skillman et al. 2003b). Errors derived from these simulations are larger than errors quoted in the literature by either assuming a constant value for the underlying absorption or derived from a χ^2 analysis in the absence of Monte Carlo simulations for the errors; Fig. 7 shows an example of these simulations for H II region A3. In Tables 5a to 5c, we included the logarithmic reddening and the equivalent width of the underlying Balmer absorption, which were solved simultaneously. Values for the logarithmic reddening are consistent with values of the reddening determined with SNAP. Where negative values were derived, the reddening was set to zero in correcting line ratios and in abundance calculations.

Relatively narrow He II emission was detected in H II regions B3 and B4. In H II region B3, the equivalent width of the He II λ 4686 emission line is 1.71 ± 0.20 Å (Fig. 8; Table 5b); the line is somewhat weaker in B4 (equivalent width 0.77 ± 0.11 Å). Using models for young stellar populations in starbursts by Schaerer & Vacca (1998), our He II data are best fit by a model with Z = 0.008, a Salpeter stellar initial mass function with upper mass limit of 120 M_{\odot} , and an instantaneous burst of star formation at an age of about 5 Myr. One can compare our data with the broad He II emission seen, for example, in the Sculptor group starburst galaxy NGC 625 (Skillman et al. 2003b).

4. Nebular Abundances

Oxygen abundances in H II regions were derived using three methods: (1) the direct method (e.g., Dinerstein 1990; Skillman 1998); and the bright-line methods discussed by (2) McGaugh (1991), which is based on photoionization models; and (3) Pilyugin (2000), which is purely empirical.

4.1. Oxygen Abundances: $[O III]\lambda$ 4363 Temperatures

For the "direct" conversion of emission line intensities into ionic abundances, a reliable estimate of the electron temperature in the ionized gas is required. H II regions are modeled as two zones: a low- and a high-ionization zone, characterized by temperatures $T_e(O^+)$ and $T_e(O^{+2})$, respectively. The temperature in the O^{+2} zone is measured with the emission line ratio $I([O III]\lambda 5007)/I([O III]\lambda 4363)$ (Osterbrock 1989). The temperature in the O^+ zone is given by

$$t_e([O II]) = 0.7 t_e([O III]) + 0.3,$$
 (4)

where $t_e = T_e/10^4$ K (Campbell et al. 1986; Garnett 1992). Within SNAP, the uncertainty in $T_e(O^{+2})$ is computed from the maximum and minimum values derived from the uncertainties in corrected emission line ratios. The computation does not include uncertainties in the reddening (if any), the uncertainties in the atomic data, or the presence of temperature fluctuations. The

uncertainty in $T_e(O^+)$ is assumed to be the same as the uncertainty in $T_e(O^{+2})$. These temperature uncertainties are conservative estimates, and are likely overestimates of the actual uncertainties. For subsequent calculations of ionic abundances, we assume the following electron temperatures (Garnett 1992): $t_e(N^+) = t_e(O^+)$, $t_e(Ne^{+2}) = t_e(O^{+2})$, and $t_e(Ar^{+2}) = 0.83$ $t_e(O^{+2}) + 0.17$.

The total oxygen abundance by number is given by $O/H = O^0/H + O^+/H + O^{+2}/H + O^{+3}/H$. For conditions found in typical H II regions and those presented here, very little oxygen in the form of O^0 is expected, and is not included here. Ionic abundances for O^+/H and O^{+2}/H were computed using O^+ and O^{+2} temperatures, respectively, as described above. He II λ 4686 Å emission is indicative of the presence of O^{+3} , which is generally a small contributor to the total oxygen abundance. For example, Kennicutt & Skillman (1993) measured He II emission in I Zw 18 and found that the resulting O^{+3} contribution was of order one to four percent. In H II region B3, He II λ 4686 Å emission is about five percent of H β . The resulting contribution by O^{+3} to the total oxygen abundance is of order 5% or 0.01 dex. Thus, the O^{+3} contribution is small and is not included in the total oxygen abundance.

Measurements of the $[O III]\lambda$ 4363 line were obtained and subsequent electron temperatures were derived in five of the 16 H II regions. Ionic abundances and total abundances are computed using the method described by Lee et al. (2003b). With SNAP, oxygen abundances were derived using the five-level atom approximation (DeRobertis et al. 1987), and transition probabilities and collision strengths for oxygen from Pradhan (1976), McLaughlin & Bell (1993), and Wiese et al. (1996). Balmer line emissivities from Storey & Hummer (1995) were used. Derived ionic and total abundances are listed in Tables 6a and 6b. These tables include derived O^+ and O^{+2} electron temperatures; O^+ and O^{+2} ionic abundances and the total oxygen abundances. Errors in direct oxygen abundances computed with SNAP have two contributions: the maximum and minimum values for abundances from errors in the temperature, and the maximum and minimum possible values for the abundances from propagated errors in the intensity ratios. These uncertainties in oxygen abundances are also conservative estimates.

Using the method described by Skillman et al. (2003b), we recompute oxygen abundances in H II regions with [O III] λ 4363 detections. Abundances are computed using the emissivities from the five-level atom program by Shaw & Dufour (1995). As described above, we use the same two-temperature zone model and temperatures for the remaining ions. The error in $T_e(O^{+2})$ is derived from the uncertainties in the corrected emission-line ratios, and does not include any uncertainties in the atomic data, or the possibility of temperature variations within the O^{+2} zone. The fractional error in $T_e(O^{+2})$ is applied similarly to $T_e(O^+)$ to compute the uncertainty in the latter. Uncertainties in the resulting ionic abundances are combined in quadrature for the final uncertainty in the total linear (summed) abundance. The adopted [O III] λ 4363 abundances and their uncertainties computed in this manner are listed in Tables 6a and 6b. Direct oxygen abundances computed with SNAP are in excellent agreement with direct oxygen abundances computed with the method described by Skillman et al. (2003b); abundances from the two methods agree to within 0.02 dex. From the five direct oxygen abundances listed, the weighted mean is $(O/H) = (1.62 \pm 0.19) \times 10^{-4}$,

or $12 + \log(O/H) = 8.21 \pm 0.05$. The mean value corresponds to [O/H] = -0.45 dex,³ or 35% of the solar value.

4.2. Oxygen Abundances: Bright-Line Methods

For H II regions without $[O III]\lambda$ 4363 measurements, secondary methods are necessary to derive oxygen abundances. The bright-line method is so called because the oxygen abundance is given in terms of the bright [O II] and [O III] lines. Pagel et al. (1979) suggested using

$$R_{23} = \frac{I([\text{O II}]\lambda \ 3727) + I([\text{O III}]\lambda\lambda \ 4959,5007)}{I(\text{H}\beta)}$$
 (5)

as an abundance indicator. Using photoionization models, Skillman (1989) showed that bright [O II] and [O III] line intensities can be combined to determine uniquely the ionization parameter and an "empirical" oxygen abundance in low-metallicity H II regions. McGaugh (1991) developed a grid of photoionization models and suggested using R_{23} and $O_{32} = I([O III]\lambda\lambda 4959,5007)/I([O II]\lambda 3727)$ to estimate the oxygen abundance. However, the calibration is degenerate such that for a given value of R_{23} , two values of the oxygen abundance are possible. The [N II]/[O II] ratio was suggested (McCall et al. 1985; McGaugh 1994; van Zee et al. 1998) as the discriminant to choose between the "upper branch" (high oxygen abundance) or the "lower branch" (low oxygen abundance). In the present set of spectra, [N II] λ 6583 line strengths are generally small, and [N II]/[O II] values have been found to be less than the threshold value of 0.1. Consequently, the lower branch is used.⁴ Pilyugin (2000) proposed a new calibration of the oxygen abundances using bright oxygen lines. At low abundances, his calibration is expressed as

$$12 + \log(O/H) = 6.35 + 3.19 \log R_{23} - 1.74 \log R_3, \tag{6}$$

where R_{23} is given by Equation (5) and $R_3 = I([O III]\lambda\lambda 4959,5007)/I(H\beta)$. In some instances, oxygen abundances with the McGaugh method could not be computed, because the R_{23} values were outside of the effective range for the models. Skillman et al. (2003b) have shown that the Pilyugin calibration covers the highest values of R_{23} . Oxygen abundances derived using the McGaugh and Pilyugin bright-line calibrations are listed in Tables 6a and 6b. For each H II region, differences between direct and bright-line abundances are shown as a function of O_{32} and R_{23} in Fig. 9. The separations between the three methods appear to increase with increasing O_{32} . The difference between the McGaugh and Pilyugin calibrations (indicated by asterisks) appears to correlate with log O_{32} , which has been previously noted by Skillman et al. (2003b) and Lee et al. (2003a). However, the values of R_{23} in the present data are near or at the maximum allowed in the McGaugh calibration, where the "kink" or the bend in the log(O/H) versus R_{23} relation occurs, and

³The following standard notation is used: $[X/H] = \log(X/H) - \log(X/H)_{\odot}$.

⁴Analytical expressions for the McGaugh calibration are found in Kobulnicky et al. (1999).

ambiguity is greatest for an estimate of the oxygen abundance (in the absence of the [N II]/[O II] discriminant). The bottom panel of Fig. 9 shows that at these values of R_{23} , the McGaugh calibration appears to give $\approx +0.2$ dex larger abundances than the Pilyugin calibration. However, we remind the reader with comments from Skillman et al. (2003b) that the McGaugh calibration does not provide sufficient range in R_{23} with his models, and the Pilyugin calibration does not include a sufficient number of low ionization H II regions. Where [O III] λ 4363 is not measured or below the detection limit, oxygen abundances derived using bright-line methods are in agreement with direct abundances to within ≈ 0.2 dex. This has obvious implications to determining nebular oxygen abundances in more distant starburst galaxies if [O III] λ 4363 cannot be detected; see also the discussion by Kobulnicky et al. (1999).

4.3. Element Ratios

For completeness, we derive nitrogen-to-oxygen, neon-to-oxygen, and argon-to-oxygen ratios, which are listed in Tables 6a and 6b. Transition probabilities and collision strengths for N⁺, Ne⁺², and Ar⁺² were taken from Mendoza (1983), Mendoza & Zeippen (1983), Butler & Zeippen (1994), Lennon & Burke (1994), Galavis et al. (1995), and Wiese et al. (1996).

For metal-poor galaxies, it is assumed that N/O \approx N⁺/O⁺ (Garnett 1990) and N⁺/O⁺ values were derived. Nitrogen abundances were computed as N/H = ICF(N) \times (N⁺/H). The ionization correction factor, ICF(N) = O/O⁺, accounts for missing ions. From H II regions A3, B3, B4, and B6, the mean (N/O) is $(1.76 \pm 0.21) \times 10^{-2}$, and the resulting log(N/O) is -1.75 ± 0.06 . The poor [N II] λ 6583 detection in H II region C6 was not included in the average. However, if the anomalously low nitrogen value in H II region B4 is ignored, the resulting means are (N/O) = $(2.34 \pm 0.33) \times 10^{-2}$, and log(N/O) = -1.63 ± 0.07 . Our N/O value is not significantly different from those obtained for other dwarf galaxies at comparable oxygen abundances (Kobulnicky & Skillman 1996; van Zee et al. 1997; Izotov & Thuan 1999).

Neon abundances are derived as Ne/H = ICF(Ne) × (Ne⁺²/H). The ionization correction factor for neon is ICF(Ne) = O/O⁺². For neon-to-oxygen ratios, we assumed Ne/O \approx Ne⁺²/O⁺² and derived a mean Ne/O of 0.374 \pm 0.028. We also obtain log(Ne/O) = -0.426 ± 0.033 , which is about 0.3 dex higher than the average for blue compact dwarf galaxies (-0.72; Izotov & Thuan 1999), but our value is at the upper end of the range for H II galaxies (Terlevich et al. 1991). These values could be too high, which might arise from problems with the reddening correction, where the $F([\text{Ne III}]\lambda 3869)/F(\text{H}\beta)$ ratio may be overcorrected. However, the unblended corrected Balmer line closest to [Ne III] λ 3869 is H δ ; the H8 Balmer line is blended with an adjacent helium line, and H ϵ is blended with [Ne III] and helium lines. Nevertheless, we find that the corrected $I(\text{H}\delta)/I(\text{H}\beta)$ and $I(\text{H}\gamma)/I(\text{H}\beta)$ ratios are consistent with the expected values.

Argon is more complex, because the dominant ion is not found in just one zone. Ar⁺² is likely to be found in an intermediate area between the O^+ and O^{+2} zones. Following the prescription

by Izotov et al. (1994), the argon abundance, was derived as $Ar/H = ICF(Ar) \times Ar^{+2}/H$. The ionization correction factor is given by $ICF(Ar) = Ar/Ar^{+2} = [0.15 + x(2.39 - 2.64x)]^{-1}$, where $x = O^+/O$. From the data for H II regions A3, B3, B4, B6 and C6, the mean (Ar/O) is $(4.8\pm1.2)\times10^{-3}$, and the resulting log(Ar/O) is -2.31 ± 0.11 . We also computed Ar^{+2}/O^{+2} , which agreed with the full derivation for the argon abundance, i.e., $Ar/O \approx Ar^{+2}/O^{+2}$. Our mean log(Ar/O) is consistent with the mean determined by Izotov & Thuan (1999) for their sample of blue compact dwarf galaxies.

5. Discussion

We present the following three points: (1) reddening measurements from the Balmer decrement are compared with previous estimates; (2) direct oxygen abundances derived from the present data are compared with previous spectroscopic measurements in the literature; and (3) simple chemical evolution models are used to compare the current state of NGC 1705 with other dwarf irregulars at comparable gas-phase metallicities.

5.1. Reddening Estimates

From their measure of the ultraviolet flux at 1400 Å, Lamb et al. (1985) claimed an upper limit for the reddening internal to the galaxy, $E(B-V)_i \lesssim 0.2$ mag. This was consistent with reddening values derived from Balmer decrements measured from the optical spectra of H II regions in similar amorphous galaxies, which were supposed to be relatively dust-free. Meurer et al. (1992) derived an upper limit to the internal reddening of $E(B-V) \lesssim 0.02$ mag from IRAS data. They also detected individual features in $H\alpha$ profiles. In particular, they were able to measure blueshifted $H\alpha$ lines, where the most blueshifted line was found to be at the center and in front of the galaxy. Thus, they concluded that one would expect zero reddening along a line of sight to the center of the galaxy. Calzetti et al. (1994) showed that the spectral slope in the ultraviolet continuum correlated with nebular extinction as measured from optical Balmer emission lines. They also found that the foreground reddening of 0.04 mag, and concluded that the intrinsic reddening within NGC 1705 was near zero. For their sample of starburst galaxies, Meurer et al. (1995) showed good correlation between the far-infrared excess and the ultraviolet spectral slope. This was best explained by a model geometry where most of the dust was in a foreground screen in near proximity of the starburst, instead of a geometry where dust was mixed with the stars; a similar conclusion was reached by Heckman et al. (1998). Observations have indicated that the reddening towards the SSC was expected to be very small, which suggests that the previous burst of star formation associated with the SSC has removed most of the dust along our line of sight to the star cluster. Schlegel et al. (1998) measured the Galactic foreground in the direction of NGC 1705 to be reddening $E(B-V)_G$ = 0.035 mag, or an extinction in V of about 0.1 mag.

As shown in Tables 5a to 5c, the derived reddenings for most of the extracted spectra are consistent with zero or very low levels of extinction. In fact, all of the H II regions observed in spectrum B are consistent (within errors) with zero reddening and spectrum B covers nebular emission over a range in galactocentric distance. The low levels of extinction are in agreement with previous estimates (Meurer et al. 1992; Heckman et al. 2001) which are primarily concerned with the line of sight to the main SSC. However, along some lines of sight, we do detect significant extinction. For example, the extinction derived for A2 is $A_V = 0.9$ mag., and the other H II regions in that vicinity also show non-zero reddening. The presence of significant and variable extinction in NGC 1705 could be important to understanding the true nature of the history of its starburst. To date, the studies of the star formation history of NGC 1705 have assumed a uniformly low value of extinction ($A_V = 0.1$; Tosi et al. 2001; Annibali et al. 2003). Since the presence of variable extinction leads to a systematic bias in the photometry of individual stars (cf. Cannon et al. 2003) and variable extinction is common in other dwarf starburst galaxies (e.g., Calzetti et al. 1999, 2000), it may be interesting to revisit the star formation history of NGC 1705 to investigate the effect that variable extinction can have on its derived star formation history.

5.2. Oxygen Abundances

5.2.1. Comparison with Previous Results

We compare our result with previous measurements of oxygen abundances published in the literature. In their optical long-slit spectrum, Lamb et al. (1985) reported bright nebular emission lines, nebular emission more extended than the stellar core, and the center of the emission displaced with respect to the stellar core. Although an oxygen abundance was not estimated, their spectrum was suggestive of a metallicity similar to that of the LMC (i.e., $12 + \log(O/H) = 8.35$; Russell & Dopita 1992). Meurer et al. (1992) reported for NGC 1705 an oxygen abundance of 12+log(O/H) ~ 8.46 , derived from bright emission line ratios in their spectrum.⁵ Storchi-Bergmann et al. (1994) and Storchi-Bergmann et al. (1995) reported gas-phase metallicities and spectra, respectively, for 44 star-forming galaxies. Although the placement of the long-slit on the galaxy is not known, their spectrum of NGC 1705 showed [O II] λ 3727 and [O III] λ 5007 emission, strong stellar continuum in the blue, but no [O III] λ 4363. With a two-zone model, they derived $T_e(O^{+2})$ and $T_e(O^{+})$ using empirical relationships between oxygen abundance and temperature from Pagel et al. (1979) and Campbell et al. (1986), respectively. The oxygen abundance was found to be $12 + \log(O/H) = 8.36$. However, with the same spectrum from Storchi-Bergmann et al. (1995), Heckman et al. (1998) used the Edmunds & Pagel (1984) bright-line calibration, and rederived a smaller value for the oxygen abundance: $12 + \log(O/H) = 8.0$. We have also taken the intensity ratios from Storchi-Bergmann et al. (1995), and we obtained $12 + \log(O/H) = 8.0$ and 7.8 using the McGaugh (1991) and Pilyugin

⁵Nebular diagnostics from the MAPPINGS code (Binette et al. 1985) were used for the derivation (G. Meurer 2004, private communication).

(2000) calibrations, respectively.

The present mean value of $12+\log(\mathrm{O/H})=8.21$ is approximately in the middle of the range of reported values (8.0 to 8.5) from the literature. When $[\mathrm{O\ III}]\lambda$ 4363 is too faint and/or not measured, one must rely on bright-line methods, where the ambiguity in choosing the appropriate "branch" for the oxygen abundance is greatest in the range of R_{23} values considered here. We have seen that there is a relatively broad range in oxygen abundances spanning about 0.7 dex when various bright-line calibrations (e.g., Pagel et al. 1979; Edmunds & Pagel 1984; McGaugh 1991; Pilyugin 2000) are considered. The present set of $[\mathrm{O\ III}]\lambda$ 4363 measurements have pinned down the nebular oxygen abundance to an accuracy of 0.1 dex. Where $[\mathrm{O\ III}]\lambda$ 4363 is unmeasurable or below the detection limit, the resulting oxygen abundances are accurate to about 0.2 dex, as Fig. 9 has shown. Fortunately, the present results do not greatly affect the conclusions about the ultraviolet properties of starburst galaxies reached by Heckman et al. (1998), or the tip of the red giant branch distance determined by Tosi et al. (2001). Tosi et al. (2001) superposed stellar evolutionary tracks on their color-magnitude diagrams, and the best agreement was reached at a metallicity Z=0.004, or about one-third solar; this is in agreement with our value of the nebular oxygen abundance.

These new nebular abundance measurements also allow us a detailed comparison with the chemical abundances measured in the neutral gas. Measurements of ultraviolet absorption lines obtained from FUSE observations have been reported by Heckman et al. (2001) and are listed in Table 7. Heckman et al. (2001) noted the very low value of N/H in the neutral gas, but concluded that most of the rest of the measured abundances were consistent with the nominal metallicity for NGC 1705. From Table 7 we see that the N/H abundance in the neutral gas is, indeed, lower than that in the nebular gas by ~ 0.7 dex. However, the O/H abundance in the neutral gas is similar to the results of other observations of dwarf galaxies (e.g., I Zw 18 - Aloisi et al. 2003, NGC 625 - Cannon & Skillman 2004). Note that the O I λ 1039.2 Å line can be at or near saturation for typical H I column densities (e.g., I Zw 18 - Lecavelier des Etangs et al. 2004) and this implies that the O/H measurement may be better interpreted as a lower limit. Nonetheless, the N/H abundances have generally been thought to be secure.

That the N/O abundance ratio in the neutral gas is essentially identical to that in ionized gas, yet the N/H and O/H are depressed by roughly a factor of five, could be taken as support for the premise that the ultraviolet absorption lines are probing a "halo" of neutral gas with a lower metallicity than the main disk of gas in NGC 1705. Note that the geometry of NGC 1705 may be most favorable for this interpretation. Although we appear to be viewing the disk of NGC 1705 face-on (Meurer et al. 1998), the extinction to the SSC is negligible and the H I column is only 1.6×10^{20} atoms cm⁻² (Heckman et al. 2001). This low column density implies that the ultraviolet absorption lines are not probing the disk gas where column densities are higher. This is in contrast to the case of I Zw 18 where the H I column density from ultraviolet absorption is more than an order of magnitude larger, and therefore almost certainly is probing the main disk gas.

Measuring the metallicity of the gas in the outer parts of dwarf galaxies remains a challenge and has important implications for the evolutionary status of dwarf galaxies (cf., Kennicutt & Skillman 2001). If a number of dwarf galaxies with characteristics similar to NGC 1705 show this trend for lower metallicity in their halo gas, then future studies of the chemical evolution of dwarf galaxies should consider modeling the metallicities with radial gradients (as is the case for spiral galaxies).

5.2.2. Spatial Variations

The spectra of H II regions in spiral galaxies have shown that oxygen abundances in spiral galaxies decrease with increasing galactocentric radii (e.g., McCall et al. 1985; Zaritsky et al. 1994; Afflerbach et al. 1996; Kennicutt et al. 2003). However, in dwarf galaxies where there is often only a single H II region, it is assumed that nebular oxygen abundances are representative of the interstellar medium metallicity for the entire galaxy. This appears to be true from extensive spectroscopic mappings of H II regions in dwarf and starburst galaxies; e.g., NGC 1569 (Devost et al. 1997; Kobulnicky & Skillman 1997), NGC 2366 (Roy et al. 1996), NGC 4214 (Kobulnicky & Skillman 1996), NGC 5253 (Kobulnicky et al. 1997), NGC 6822 (Pagel et al. 1980; Lee, Skillman, & Venn, in preparation). Kobulnicky & Skillman (1997) discussed scenarios to explain flat chemical abundance profiles seen on spatial scales between $\gtrsim 10$ pc and $\lesssim 1$ kpc in low-mass galaxies. A possible explanation is that freshly produced chemical elements from are dispersed or transported very quickly to all regions of the galaxy and are well mixed very quickly as well on small scales within the interstellar medium. However, the timescales required for both dispersal and mixing must be less than 10⁷ yr. The most plausible scenario is that newly synthesized heavy elements are not yet mixed with the surrounding gas in the interstellar medium, and that these fresh metals reside in relatively hot 10⁶ K gas or in cold molecular gas. Both of these phases are at present difficult to detect.

The metallicity for the SSC was found to be about one-half solar, or $12+\log(O/H) \sim 8.4$, but this appears only to be a rough estimate (Vázquez et al. 2004). The presence of massive star clusters should be able to provide substantial localized chemical enrichment (see § 5 in Kobulnicky & Skillman 1997 and references therein). H II regions where $[O\ III]\lambda$ 4363 measurements were presented above are distributed in a radius of about 10'' from the SSC. From the present data, direct oxygen abundances are in the range between $12+\log(O/H)=8.17$ and 8.29. Individual variations (0.04 to 0.08 dex) for H II region abundances about the weighted mean are comparable with the 0.05 dex uncertainty computed for the mean. This suggests a lack of spatial variations in oxygen abundances for H II regions where $[O\ III]\lambda$ 4363 was measured. This is consistent with similar conclusions for other dwarf galaxies; for example, in the post-starburst galaxy NGC 1569 (Kobulnicky & Skillman 1997).

We note with interest that *Chandra* observations of NGC 1569 by Martin et al. (2002) have revealed the existence of metals-enriched winds in the hot gas phase, and that the wind has carried nearly all of the metals ejected by the recent starburst. As Kobulnicky & Skillman (1997) suggest,

we may be seeing good dispersal of newly synthesized metals from the recent starburst into the interstellar medium, but not necessarily good mixing of the metals in the various gas phases within dwarf galaxies. Instantaneous recycling is questionable as an appropriate assumption in simple models of chemical evolution; see also the discussion in Kobulnicky & Skillman (1997). It is puzzling why we happen to be seeing spatial homogeneity in nebular oxygen abundances at this very time, especially if the metallicity of the most recent starburst in the SSC is indeed confirmed to be higher than that of the nebular phase. It will be interesting to see if *Chandra* observations can shed any light on the metallicity of the hot gas phase, although NGC 1705 may be too faint in X-ray luminosity to place useful constraints.

5.3. Evolution of NGC 1705

From the H α flux reported by Gil de Paz et al. (2003) (see Table 1), the total H α luminosity is $L(\text{H}\alpha) = 7.9 \times 10^{39} \text{ ergs s}^{-1}$. Using the formulation by Kennicutt et al. (1994), the H α luminosity is converted to the total current star formation rate (SFR) as

SFR =
$$\frac{L(H\alpha)}{1.26 \times 10^{41} \text{ ergs s}^{-1}} M_{\odot} \text{ yr}^{-1}$$
. (7)

This gives an SFR equal to $0.06 \text{ M}_{\odot} \text{ yr}^{-1}$. The star formation rate per unit luminosity is given by SFR/ $L_B = 2.3 \times 10^{-10} \text{ M}_{\odot} \text{ yr}^{-1} \text{ L}_{\odot,B}^{-1}$. The formation timescale is thus $L_B/\text{SFR} = 4.3 \text{ Gyr}$. The gas depletion timescale is given by the ratio of the total gas mass (1.3 M_{HI} to account for helium) to the SFR, and is equal to 2.1 Gyr. The consumption and formation timescales are much lower than normal irregulars (e.g., Skillman et al. 2003a), but this is not surprising, if the burst in NGC 1705 is a large contributor to the luminosity in B.

The metallicity-luminosity diagram has been known as being representative of a relationship between metallicity and stellar mass for dwarf irregular galaxies (e.g., Skillman et al. 1989; Richer & McCall 1995; Lee et al. 2003b; Skillman et al. 2003b). The measured oxygen abundance and B luminosity for NGC 1705 are consistent with the relation defined by nearby dwarf irregular galaxies (Fig. 10). Lee et al. (2003c) noted that oxygen abundances for dwarf irregulars in the Virgo Cluster were comparable to a local sample of dwarf irregulars at a given luminosity. The metallicity-luminosity diagram for dwarf irregulars appears relatively unchanged by the cluster environment, although it is thought that dwarf galaxies should be affected by both external (e.g., tidal and/or ram-pressure stripping) and internal (e.g., blowout) mechanisms. NGC 1705 is a relatively isolated galaxy, and Fig. 10 shows that the current state of the galaxy in the metallicity-luminosity diagram appears relatively unaffected by the internal trauma caused by the recent starburst.

However, if the data point for NGC 1705 is indeed above and to the left of the best-fit line shown in the Figure, possible scenarios to account for the apparent offset include constant star formation rate (to boost the metallicity at a given luminosity), pure fading (to decrease the luminosity at a given metallicity), or both (e.g., Fig. 9 in Kobulnicky et al. 2003). Observations of the SSC

have shown that star formation ceased ≈ 10 Myr ago, but any fading in 10 Myr is negligible. For example, timescales of order 1 Gyr are required for passive fading by about 1 mag (e.g., Bothun 1982). Annibali et al. (2003) have shown that continuous star formation with a variable rate can explain the age mixture of stellar populations observed in their HST photometry. If we assume a roughly constant (integrated over the last ≈ 1 Gyr) rate of star formation, it is possible that star formation has supplied additional metals to explain how the nebular oxygen abundance for NGC 1705 may be higher than expected compared to local dwarfs at similar luminosity. On the other hand, there may be no offset and, because of the relatively small number of galaxies shown in the plot, this may simply be due to scatter in the metallicity-luminosity diagram.

Dwarf galaxies can experience large outflows, which has been observed in NGC 1705 (Meurer et al. 1992; Marlowe et al. 1995; Heckman et al. 2001). We examine the effects on the current gas fraction, which is a key parameter in models of chemical evolution (e.g., Pagel 1997). For the simple closed-box model, the fraction of gas mass in the form of metals (in this case, oxygen), Z_O , is given by

$$Z_O = y_O \ln(1/\mu),\tag{8}$$

where y_O is the mass fraction of metals in the form of oxygen, and μ is the gas fraction, which is the ratio of gas mass to the total mass in gas and stars. The yield is usually referred as the "effective yield" if the assumptions in the closed-box model are not appropriate (e.g., Edmunds 1990; Garnett 2002). The total gas mass is usually the H I gas mass multiplied by a constant (1.3) to account for helium; the molecular and ionized gas masses are assumed to be small. Baryonic gas fractions also require knowledge of stellar masses. A constant stellar mass to light ratio is usually applied, although there may be some variation from galaxy to galaxy; see, e.g., Bell & de Jong (2001) and Lee et al. (2003b). We consider here the gas to light ratio, $M_{\rm HI}/L_B$, as a proxy for the gas fraction. The advantages of using the gas-to-light ratio are: the ratio is constructed from purely observed quantities, and the ratio is independent of distance.

Figure 11 shows a plot of oxygen abundance versus the H I gas to B light ratio for dwarf galaxies. It is clear from this diagram that there is a rough correlation among dwarf galaxies where oxygen abundances increase with decreasing gas to light ratios, as expected for normal astration. Local dwarfs, Sculptor group dwarfs, a number of more distant dwarfs in the field, and the nearby gas-rich dwarf DDO 154 are all plotted for comparison (Kobulnicky et al. 1997; van Zee et al. 1997; Kennicutt & Skillman 2001; Lee et al. 2003b; Skillman et al. 2003b). Skillman et al. (2003b) already noted that a number of isolated dwarfs in the field and DDO 154 are best fit by a model with effective yield by mass equal to 4.9×10^{-3} . This corresponds to about 90% of the solar value. At low oxygen abundance, a number of local dwarfs appear to have lower than expected $M_{\rm HI}/L_B$ values at a given metallicity. The bottom (dashed) curve is an arbitrary fit to the lower envelope of the locus for nearby dwarfs; the effective yield in this case is about 12% of the solar value. The lower gas-to-light ratios could arise from (a) lower gravitational potentials, which are unable to retain metals, and/or (b) the effect of a recent burst which contributes to the luminosity in B.

The "current" state of NGC 1705 puts this galaxy in similar phase space with the locus of

local dwarfs at the upper range of oxygen abundances. Adopting a stellar mass to light ratio equal to 1.2, the model which fits NGC 1705 has an effective yield equal to 1.6×10^{-3} , or about 30% of the solar value. Comparing to the sample of field dwarf irregulars with near-solar yields at a similar oxygen abundance, it is possible that NGC 1705 has experienced previous gas loss to reduce the effective yield from near solar to one-third solar. Heckman et al. (2001) suggested a scenario that most of the H I gas would be retained in the galaxy, but most of the hot gas driving the outflow would escape the galaxy. Mass loss (with the depletion timescale as a rough indicator) will eventually convert this galaxy into a gas-poor dwarf with an enhanced stellar core (i.e., the SSC).

One must be cautious about overinterpreting the results. Although there is significant scatter in Fig. 11, one might ask about the significance of the positions of IC 5152, NGC 625, NGC 1569, and NGC 5253 with respect to NGC 1705. All of the galaxies shown could simply be a part of the overall distribution of galaxies with similar abundances and a wide range in $M_{\rm HI}/L_B$. Optical colors for the galaxies shown are similar with a range of B-V from about 0.4 to 0.8; indeed, it is very difficult to spot a real trend or to pick out "outliers" on the basis of their color. For the five galaxies, their H I masses are all roughly the same (between 1.0 and 1.3 $\times 10^8$ M_{\odot}), and their total B luminosities, log L_B , are in the range between 8.4 and 9.1.

Could the total blue luminosity be biased by the recent burst of star formation (i.e., SSC)? The optical luminosity of the SSC is $M_{\text{cl},B} = -13.6$ (Smith & Gallagher 2001). The relative contribution of B luminosity by the SSC to the total galaxy luminosity is about 16%, which is in contrast with the ultraviolet where the SSC contributes $\sim 50\%$ of the total emission (Meurer et al. 1995; Heckman & Leitherer 1997). Because NGC 1705 is close to face-on and the line of sight to the SSC is not extincted, one expects that other starburst galaxies with edge-on inclinations should have smaller relative contributions by their respective star clusters to the total optical B luminosities. We see that the luminosity contribution by the recent starburst to the total optical light is not negligible. Gathering a sample of galaxies with infrared fluxes would be worthwhile (1) to judge properly the underlying stellar mass, which has been shown to be a better indicator of evolution for star-forming galaxies than luminosity (Tremonti et al. 2004), and (2) to reduce the scatter caused by recent bursts of star formation. In particular, a comparison between relatively quiescent dwarf irregulars with dwarf starburst galaxies would be illuminating.

6. Conclusions

Optical long-slit spectra have been obtained for 16 H II regions in NGC 1705. [O III] λ 4363 is detected in five H II regions, and the resulting oxygen abundances are between 12+log(O/H) = 8.17 and 8.29. We adopt a mean value of 12+log(O/H) = 8.21 ± 0.05, corresponding to [O/H] = -0.45, or 35% of the solar value. There is no significant spatial variation of [O III] λ 4363 abundances (\lesssim 0.10 dex) in H II regions distributed in a radius of \approx 10" from the super star cluster. Bright-line calibrations are used to derive oxygen abundances in the remaining H II regions without [O III] λ 4363 measurements; bright-line oxygen abundances are accurate only to within

 $0.2~{
m dex}$. The mean argon- and nitrogen-to-oxygen abundance ratios are consistent with average values for blue compact dwarf galaxies and other samples of dwarf irregular galaxies. The mean neon-to-oxygen ratio for NGC 1705 is about a factor of two larger than the value for blue compact dwarf galaxies, although the present value is still in the range of values for H II galaxies. The nitrogen-to-oxygen ratio in the ionized H II gas is in agreement with the value for neutral H I, even though the metallicity of the neutral gas may be as much as six times lower than that of the ionized gas. From observed Balmer flux ratios, derived values of the extinction in V, A_V , are in the range zero to 0.9 mag along various lines of sight to H II regions in the galaxy. One may need to take into account possible spatial variations in extinction to correct properly the photometry of resolved stars, which can affect the derived history of star formation. The position of NGC 1705 on metallicity-B luminosity and metallicity-gas fraction plots shows that the adopted oxygen abundance is comparable to Local Group dwarf irregulars at comparable luminosity and gas fraction. In combination with existing observations, simple chemical evolution models suggest that NGC 1705 may be quickly evolving into a gas-poor dwarf galaxy.

We thank the anonymous referee for comments which improved the presentation of this paper. We thank Alessandra Aloisi for suggesting this project and providing valuable comments, Ken Sembach and John Cannon for additional comments, and Tim Heckman, Gerhardt Meurer, and Dave Strickland for helpful communications. H. L. also thanks Lisa Germany and the staff at ESO La Silla for their help with the observations. H. L. and E. D. S. acknowledge partial support from a NASA LTSARP grant NAG 5–9221 and the University of Minnesota. This research has made use of NASA's Astrophysics Data System, and of the NASA/IPAC Extragalactic Database (NED), which is operated by the Jet Propulsion Laboratory, California Institute of Technology, under contract with the National Aeronautics and Space Administration.

Facilities: ESO(EFOSC2)

REFERENCES

- Afflerbach, A., Churchwell, E., Acord, J. M., Hofner, P., Kurtz, S., & Depree, C. G. 1996, ApJS, 106, 423
- Aller, L. H. 1984, Physics of Thermal Gaseous Nebulae (Dordrecht: Reidel)
- Aloisi, A., Savaglio, S., Heckman, T. M., Hoopes, C. G., Leitherer, C., & Sembach, K. R. 2003, ApJ, 595, 760
- Annibali, F., Greggio, L., Tosi, M., Aloisi, A., & Leitherer, C. 2003, AJ, 126, 2752
- Asplund, M., Grevesse, N., Sauval, A. J., Allende Prieto, C., & Kiselman, D. 2004, A&A, 417, 751
- Bell, E. F., & de Jong, R. 2001, ApJ, 550, 212
- Binette, L., Dopita, M. A., & Tuohy, I. R. 1985, ApJ, 297, 476
- Bothun, G. D. 1982, ApJS, 50, 39
- Butler, K., & Zeippen, C. J. 1994, A&AS, 108, 1
- Calzetti, D., Kinney, A. L., & Storchi-Bergmann, T. 1994, ApJ, 429, 582
- Calzetti, D., Conselice, C. J., Gallagher, J. S., & Kinney, A. L. 1999, AJ, 118, 797
- Calzetti, D., Armus, L., Bohlin, R. C., Kinney, A. L., Koornneef, J., & Storchi-Bergmann, T. 2000, ApJ, 533, 682
- Calzetti, D., Harris, J., Gallagher, J. S., Smith, D. A., Conselice, C. J., Homeier, N., & Kewley, L. 2004, AJ, 127, 1405
- Campbell, A., Terlevich, R. J., & Melnick, J. 1986, MNRAS, 223, 811
- Cannon, J. M., Dohm-Palmer, R. C., Skillman, E. D., Bomans, D. J., Côté, S., & Miller, B. W. 2003, AJ, 126, 2806
- Cannon, J. M., & Skillman, E. D. 2004, ApJ, submitted
- Cardelli, J. A., Clayton, G. C., & Mathis, J. S. 1989, ApJ, 345, 245
- DeRobertis, M. M., Dufour, R. J., & Hunt, R. W. 1987, JRASC, 81, 195
- Devost, D., Roy, J.-R., & Drissen, D. 1997, ApJ, 482, 765
- Dinerstein, H. L. 1990, in The Interstellar Medium in Galaxies, ed. H. A. Thronson & J. M. Shull (Dordrecht: Kluwer), 257
- Edmunds, M. G. 1990, MNRAS, 246, 678

Edmunds, M. G., & Pagel, B. E. J. 1984, MNRAS, 211, 507

Galavis, M. E., Mendoza, C., & Zeippen, C. J. 1995, A&AS, 111, 347

Garnett, D. R. 1990, ApJ, 363, 142

Garnett, D. R. 1992, AJ, 103, 1330

Garnett, D. R. 2002, ApJ, 581, 1019

Gil de Paz, A., Madore, B. F., & Pevunova, O. 2003, ApJS, 147, 29

Greve, A., Becker, R., Johansson, L. E. B., & McKeith, C. D. 1996, A&A, 312, 391

Heckman, T. M., & Leitherer, C. 1997, AJ, 114, 69

Heckman, T. M., Robert, C., Leitherer, C., Garnett, D. R., & van der Rydt, F. 1998, ApJ, 503, 646

Heckman, T. M., Sembach, K. R., Meurer, G. R., Strickland, D. K., Martin, C. L., Calzetti, D., & Leitherer, C. 2001, ApJ, 554, 1021

Hensler, G., Dickow, R., Junkes, N., & Gallagher, J. S. 1998, ApJ, 502, L17

Ho, L. C., & Filippenko, A. V. 1996, ApJ, 472, 600

Hoopes, C. G., Sembach, K. R., Heckman, T. M., Meurer, G. M., Aloisi, A., Calzetti, D., Leitherer, C., & Martin, C. L. 2004, ApJ, in press (astro-ph/0406378)

Hunter, D. A., Hawley, W. N., & Gallagher, J. S. 1993, AJ, 106, 1797

Izotov, Y. I., & Thuan, T. X. 1999, ApJ, 511, 639

Izotov, Y. I., Thuan, T. X., & Lipovetsky, V. A. 1994, ApJ, 435, 647

Johnson, K. E., Indebetouw, R., & Pisano, D. J. 2003, AJ, 126, 101

Kauffmann, G., White, S. D. M., & Guiderdoni, B. 1993, MNRAS, 264, 201

Kennicutt, R. C., & Skillman, E. D. 1993, ApJ, 411, 655

Kennicutt, R. C., & Skillman, E. D. 2001, AJ, 121, 1461

Kennicutt, R. C., Tamblyn, P., & Congdon, C. W. 1994, ApJ, 435, 22

Kennicutt, R. C., Bresolin, F., & Garnett, D. R. 2003, ApJ, 591, 801

Kewley, L. J. & Dopita, M. A. 2002, ApJS, 142, 35

Kobulnicky, H. A., & Skillman, E. D. 1996, ApJ, 471, 211

Kobulnicky, H. A., & Skillman, E. D. 1997, ApJ, 489, 636

Kobulnicky, H. A., Skillman, E. D., Roy, J., Walsh, J. R., & Rosa, M. R. 1997, ApJ, 477, 679

Kobulnicky, H. A., Kennicutt, R. C. Jr., & Pizagno, J. L. 1999, ApJ, 514, 544

Kobulnicky, H. A., Willmer, C. N. A., Phillips, A. C., Koo, D. C., Faber, S. M., Weiner, B. J., Sarajedini, V. L., Simard, L., & Vogt, N. P. 2003, ApJ, 599, 1006

Krawchuk, C. A. P., McCall, M. L., Komljenovic, M., Kingsburgh, R., Richer, M. G., & Stevenson, C. 1997, in IAU Symp. 180, Planetary Nebulae, ed. H. J. Habing & H. J. G. L. M. Lamers (Dordrecht: Kluwer), 116

Lamb, S. A., Hjellming, M. S., Gallagher, J. S., & Hunter, D. A. 1985, ApJ, 291, 63

Lebouteiller, V., Kunth, D., Lequeux, J., Lecavelier des Etangs, A., Désert, J.-M., Hébrard, G., & Vidal-Madjar, A. 2004, A&A, 415, 55

Lecavelier des Etangs, A., Désert, J.-M., Kunth, D., Vidal-Madjar, A., Callejo, G., Ferlet, R., Hébrard, G., & Lebouteiller, V. 2004, A&A, 413, 131

Lee, H. 2001, Ph.D. thesis, York University

Lee, H., Grebel, E. K., & Hodge, P. W. 2003a, A&A, 401, 141

Lee, H., McCall, M. L., Kingsburgh, R., Ross, R., & Stevenson, C. C. 2003b, AJ, 125, 146

Lee, H., McCall, M. L., & Richer, M. G. 2003c, AJ, 125, 2975

Lennon, D. J., & Burke, V. M. 1994, A&AS, 103, 273

Marlowe, A. T., Heckman, T. M., Wyse, R. F. G., & Schommer, R. 1995, ApJ, 438, 563

Marlowe, A. T., Meurer, G. R., Heckman, T. M., & Schommer, R. 1997, ApJS, 112, 285

Martin, C. L., Kobulnicky, H. A., & Heckman, T. M. 2002, ApJ, 574, 663

Mateo, M. 1998, ARA&A, 36, 435

McCall, M. L., Rybski, P. M., & Shields, G. A. 1985, ApJS, 57, 1

McGaugh, S. S. 1991, ApJ, 380, 140

McGaugh, S. S. 1994, ApJ, 426, 135

McLaughlin, B. M., & Bell, K. L. 1993, ApJ, 408, 753

Melnick, J., Moles, M., Terlevich, R. 1985, A&A, 149, L24 (MMT85)

Mendoza, C. 1983, in IAU Symp. 103, Planetary Nebulae, ed. D. R. Flower (Dordrecht: Reidel), 143

Mendoza, C., & Zeippen, C. J. 1983, MNRAS, 202, 981

Meurer, G. R., Freeman, K. C., & Dopita, M. A. 1989. Ap&SS, 156, 141

Meurer, G. R., Freeman, K. C., Dopita, M. A., & Cacciari, C. 1992, AJ, 103, 60 (MFDC92)

Meurer, G. R., Heckman, T. M., Leitherer, C., Kinney, A., Robert, C., & Garnett, D. R. 1995, AJ, 110, 2665

Meurer, G. R., Staveley-Smith, L., & Killeen, N. E. B. 1998, MNRAS, 300, 705

O'Connell, R. W., Gallagher, J. S., & Hunter, D. A. 1994, ApJ, 433, 65

Olive, K. A., & Skillman, E. D. 2001, New A, 6, 119

Osterbrock, D. E. 1989, Astrophysics of Gaseous Nebulae and Active Galactic Nuclei (Mill Valley: University Science Books)

Pagel, B. E. J., Edmunds, M. G., Blackwell, D. E., Chen, M. S., & Smith, G. 1979, MNRAS, 189, 95

Pagel, B. E. J., Edmunds, M. G., & Smith, G. 1980, MNRAS, 193, 219

Pagel, B. E. J. 1997, Nucleosynthesis and the Chemical Evolution of Galaxies (Cambridge: Cambridge University Press)

Pilyugin, L. S. 2000, A&A, 362, 325

Pradhan, A. K. 1976, MNRAS, 177, 31

Quillen, A. C., Ramírez, S. V., & Frogel, J. A. 1995, AJ, 110, 205

Richer, M. G., & McCall, M. L. 1995, ApJ, 445, 642

Roy, J., Belley, J., Dutil, Y., & Martin, P. 1996, ApJ, 460, 284

Russell, S. C., & Dopita, M. A. 1992, ApJ, 384, 508

Sahu, M. S. 1998, AJ, 116, 1205

Sahu, M. S., & Blades, J. C. 1997, ApJ, 484, L125

Schaerer D., & Vacca W.D., 1998, ApJ, 497, 168

Schlegel, D. J., Finkbeiner, D. P., & Davis, M. 1998, ApJ, 500, 525

Shaw, R. A., & Dufour, R. J. 1995, PASP, 107, 896

- Skillman, E. D. 1989, ApJ, 347, 883
- Skillman, E. D. 1998, in Stellar Astrophysics of the Local Group: VIII Canary Islands Winter School of Astrophysics, ed. A. Aparicio, A. Herrero, & F. Sánchez (Cambridge Univ. Press), 457
- Skillman, E. D., Kennicutt, R. C., & Hodge, P. 1989, ApJ, 347, 875
- Skillman, E. D., Côté, S., & Miller, B. W. 2003a, AJ, 125, 593
- Skillman, E. D., Côté, S., & Miller, B. W. 2003b, AJ, 125, 610
- Skillman, E. D., Tolstoy, E., Cole, A. A., Dolphin, A. E., Saha, A., Gallagher, J. S., Dohm-Palmer, R. C., & Mateo, M. 2003c, ApJ, 596, 253
- Smith, L. J., & Gallagher, J. S. 2001, MNRAS, 326, 1027
- Storchi-Bergmann, T., Calzetti, D., & Kinney, A. L. 1994, ApJ, 429, 572
- Storchi-Bergmann, T., Kinney, A. L., & Challis, P. 1995, ApJS, 98, 103
- Storey, P. J., & Hummer, P. J. 1995, MNRAS, 272, 41
- Suchkov, A. A., Balsara, D. S., Heckman, T. M., & Leitherer, C. 1994, ApJ, 430, 511
- Terlevich, R., Melnick, J., Masegosa, J., Moles, M., & Copetti, M. V. F. 1991, A&AS, 91, 285
- Tosi, M., Sabbi, E., Bellazzini, M., Aloisi, A., Greggio, L., Leitherer, C., & Montegriffo, P. 2001, AJ, 122, 1271
- Tremonti, C. A., Leitherer, C., Calzetti, D., & Heckman, T. 2001, in Starburst Galaxies: Near and Far, ed. L. Tacconi & D. Lutz (Springer: Berlin), 278
- Tremonti, C. A., Heckman, T. M., Kauffmann, G., Brinchmann, J., Charlot, S., White, S. D. M., Seibert, M., Peng, E. W., Schlegel, D. J., Uomoto, A., Fukugita, M., & Brinkmann, J. 2004, ApJ, in press (astro-ph/0405537)
- van Zee, L., Haynes, M. P., & Salzer, J. J. 1997, AJ, 114, 2479
- van Zee, L., Salzer, J. J., Haynes, M. P., O'Donoghue, A. A., & Balonek, T. J. 1998, AJ, 116, 2805
- Vázquez, G. A., Leitherer, C., Heckman, T. M., Lennon, D. J., de Mello, D. F., Meurer, G. R., & Martin, C. L. 2004, ApJ, 600, 162
- Wiese, W. L., Fuhr, J. R., & Deters, T. M. 1996, Atomic transition probabilities of carbon, nitrogen, and oxygen: a critical data compilation (American Chemical Society for the National Institute of Standards and Technology)

York, D. G., Caulet, A., Rybski, P., Gallagher, J., Blades, J. C., Morton, D. C., & Wamsteker, W. 1990, ApJ, 351, 412

Zaritsky, D., Kennicutt, R. C., & Huchra, J. P. 1994, ApJ, 420, 87

This preprint was prepared with the AAS $\mbox{\sc IAT}_{\mbox{\sc EX}}\mbox{\sc X}$ macros v5.2.

- Fig. 1.— Long-slit orientations in NGC 1705 using the $H\alpha$ image adapted from Gil de Paz et al. (2003, their Fig. 3). Black objects on the image indicate bright sources. The field shown in the left frame is 1.56×1.70 . The contrast is adjusted to highlight both bright and faint $H\alpha$ emission. The central 0.78×0.85 is indicated as a box and is shown in the right frame. H II regions where $[O\ III]\lambda$ 4363 is detected are labelled. In both frames, north and east are to the top and the left, respectively. The position of the super star cluster (SSC) is indicated (Melnick et al. 1985; Meurer et al. 1989); the SSC has been blanked out of the $H\alpha$ image.
- Fig. 2.— Two-minute acquisition image in H α with EFOSC2 for the slit A configuration. Black objects on the image indicate bright sources. The separation between the solid lines corresponds approximately to the 1".5 slit width projected on the sky. Labeled are H II regions for which spectra were obtained. In the right panel, the image is rescaled to emphasize H II regions A1, A2, and A4.
- Fig. 3.— Two-minute acquisition image in H α for the slit B configuration. The aperture for H II region B4 encompassed H II regions B3 and B5. H II region B8 corresponds to the bright feature in an H α arc to the northeast; this is also seen as a bright clump in the arc "A7" in Meurer et al. (1992); see also Gil de Paz et al. (2003). In the right panel, the image is rescaled to emphasize H II regions B1, B7, and B8. See Fig. 2 for additional comments.
- Fig. 4.— Two-minute acquisition image in H α for the slit C configuration. The aperture for H II region C2 encompassed H II regions C1 and C3. See Fig. 2 for additional comments.
- Fig. 5.— Emission-line spectra between 3600 and 7300 Å. The observed flux per unit wavelength is plotted versus wavelength. The bottom panel in each part is displayed to highlight fainter emission lines, especially [O III] λ 4363 as indicated. (a) H II region A3. (b) H II region B3. (c) H II region B6. (d) H II region C6.
- Fig. 6.— Spectrum of aperture C5, which is the super star cluster (SSC) first discussed by Melnick et al. (1985) and Meurer et al. (1989). The top panel shows the spectrum from 3600 to 7300 Å; note the weak [O III] $\lambda\lambda$ 4959,5007 and H α emission. The middle and bottom panels show the spectrum from 3600 to 5500 Å, and from 5500 to 7300 Å, respectively.
- Fig. 7.— Monte Carlo simulations of solutions for the reddening, $c(H\beta)$, and the underlying Balmer absorption with equivalent width, EW_{abs} , from hydrogen Balmer flux ratios. Dotted lines mark zero values for each quantity. The results here are shown for the H II region A3. Each small point is a solution derived from a different realization of the same input spectrum. The large filled circle with error bars shows the mean result with 1σ errors derived from the dispersion in the solutions.
- Fig. 8.— Spectrum of H II region B3 in the region between 4300 and 4800 Å. Highlighted are emission lines $H\gamma$, [O III] λ 4363, He I λ 4471, and He II λ 4686.

Fig. 9.— Difference in oxygen abundance from various methods versus log O_{32} (top panel), and versus log R_{23} (bottom panel). Each point represents an H II region. "Direct" denotes oxygen abundances derived using the bright-line method by McGaugh (1991), and "P00" denotes oxygen abundances derived using the bright-line method by Pilyugin (2000). Vertical dotted lines in both panels mark zero differences in oxygen abundance. In the bottom panel, we list in the legend the dispersion in the differences for each method used to derive oxygen abundances. These plots show that oxygen abundances derived with bright-line methods are accurate only to within ≈ 0.2 dex.

Fig. 10.— Oxygen abundance versus absolute magnitude in B for dwarf irregular galaxies. Only galaxies with $[O\ III]\lambda$ 4363 detections are shown. An open star marks the location of NGC 1705. A sample of local dwarf irregular galaxies is marked by solid circles and the solid line is a fit to these galaxies (Lee et al. 2003b; Kobulnicky et al. 1997). The "Y" symbols are dwarf irregulars from the Sculptor group (Skillman et al. 2003a,b). Open triangles indicate a sample of dwarf irregulars in the field (van Zee et al. 1997). DDO 154 (van Zee et al. 1997; Kennicutt & Skillman 2001) is marked by an open square. For its luminosity, the oxygen abundance of NGC 1705 is comparable to other dwarf irregulars.

Fig. 11.— Oxygen abundance versus H I gas-to-light ratio for dwarf irregular galaxies. The symbols are the same as in Fig. 10. Chemical evolution models shown are as follows: dotted line - model to fit DDO 154 (Kennicutt & Skillman 2001); thick solid line - an approximate fit to NGC 1705; dashed line - ad hoc lower envelope for the locus defined by dwarfs in this plot. A constant stellar mass to light ratio, $M_*/L_B = 1.2$, was adopted for all models. The effective oxygen yield by mass, $y_{\rm O}$, for each model is also given. Although NGC 1705 is known to be isolated, the galaxy has a gas-to-light ratio comparable with values for other dwarf irregulars in group environments at a given oxygen abundance.

Table 1: Basic data for NGC 1705.

	Property	Value	References
(1)	Type	amorphous; BCD,N	1, 2
(2)	$F_{21} \; (\mathrm{Jy} \; \mathrm{km} \; \mathrm{s}^{-1})$	16.6	2
(3)	D (Mpc)	5.1 ± 0.6	3
(4)	Scale (pc $arcsec^{-1}$)	25	4
(5)	$v_{\odot} \; (\mathrm{km} \; \mathrm{s}^{-1})$	628 ± 9	5
(6)	$v_{\rm rot}~({\rm km~s^{-1}})$	62	5
(7)	$r_{\exp,B}$ (")	13.6	6
(8)	$\mu_{0,B} \; (\mathrm{mag \; arcsec^{-2}})$	20.86	6
(9)	B (mag)	13.09 ± 0.01	7
(10)	B - R (mag)	0.90 ± 0.06	7
(11)	$F(\mathrm{H}\alpha)~(\mathrm{ergs~s^{-1}~cm^{-2}})$	$(2.53 \pm 0.03) \times 10^{-12}$	7
(12)	$L_{\rm UV}~{ m (ergs~s^{-1})}$	7.4×10^{41}	8
(13)	$L_{\rm X}~{\rm (ergs~s^{-1})}$	1.2×10^{38}	9
(14)	$E(B-V)_G \text{ (mag)}$	+0.035	10
(15)	$E(B-V)_{\rm i}~({\rm mag})$	0.00	11
(16)	$M_B \text{ (mag)}$	-15.6	4
(17)	$M_{ m HI}~({ m M}_{\odot})$	1.0×10^8	4
(18)	$\logM_{ m HI}/L_B$	-0.42	4
(19)	$12 + \log(\mathrm{O/H})$	8.21 ± 0.05	4

Note. — Properties. (1) Morphological type. (2) 21-cm flux integral. (3) Distance. (4) Linear to angular scale at this distance. (5) Systemic heliocentric velocity in the optical. (6) Maximum H I rotational velocity. (7) Exponential scale length in B. (8) Uncorrected central surface brightness in B. (9) Apparent total magnitude in B. (10) Measured total B-R color. (11) Integrated H α flux, corrected for underlying Balmer absorption with equivalent width 3 Å. (12) Total ultraviolet luminosity. (13) Total X-ray luminosity (soft). (14) Reddening from the Galactic foreground. (15) Reddening intrinsic to NGC 1705. (16) Absolute magnitude in B, corrected for $E(B-V)_G$. (17) H I gas mass. (18) Logarithm of the H I-mass to blue luminosity ratio. (19) Mean oxygen abundance from H II regions.

References. — 1. Marlowe et al. (1995); 2. Meurer et al. (1992); 3. Tosi et al. (2001); 4. present work; 5. Meurer et al. (1998); 6. Marlowe et al. (1997); 7. Gil de Paz et al. (2003); 8. Heckman et al. (1998); 9. Hensler et al. (1998); 10. Schlegel et al. (1998); 11. Calzetti et al. (1994).

Table 2: Properties of EFOSC2 spectrograph employed at the ESO La Silla 3.6-m telescope.

	222 (11 - 2)				
Loral	CCD (#40)				
Total area	$2048~\mathrm{pix} \times 2048~\mathrm{pix}$				
Field of view	$5.2~\mathrm{arcmin}~\times~5.2~\mathrm{arcmin}$				
Pixel size	$15~\mu\mathrm{m}$				
Image scale	$0.16 \mathrm{arcsecpixel^{-1}}$				
Gain	$1.3 e^{-} ADU^{-1}$				
Read-noise (rms)	$9~e^-$				
Long slit					
Length	$\simeq 5 \text{ arcmin}$				
Width	1.5 arcsec				
Gra	ating #11				
Groove density	$300 \text{ lines mm}^{-1}$				
Blaze λ (1st order)	$4000~{\rm \AA}$				
Dispersion	$2.04 \text{ Å pixel}^{-1}$				
Effective λ range	3380 – 7520 Å				

Table 3. Log of Observations.

Slit (1)	Date (UT 2003) (2)	$\alpha \text{ (J2000)}$ $\binom{h \ m \ s}{3}$	δ (J2000) (° ' '') (4)	PA (°) (5)	N_{exp} (6)	t_{total} (s) (7)	$\langle X \rangle$ (8)	[O III]λ 4363 (9)	RMS (mag) (10)
A	27 Aug	04 54 17.0	-53 21 34.0	275°.0	3×1200 1×1200 1×1200	3600	1.21	A3	0.029
B	28 Aug	04 54 15.4	-53 21 39.4	358°.1		1200	1.18	B3, B4, B6	0.034
C	28 Aug	04 54 16.2	-53 21 17.7	243°.2		1200	1.18	C6	0.034

Note. — Col. (1): Slit orientation, as shown in Fig. 1. Col. (2): Date. Cols. (3) and (4): Center of the long-slit in right ascension and declination (Epoch J2000). Col. (5): Position angle, north through east. Col. (6): Number of exposures obtained and the length of each exposure in seconds. Col. (7): Total exposure time. Col. (8): Mean effective airmass. Col. (9): H II regions where [O III] λ 4363 detected; see Table 4. Col. (10): Relative root–mean–square error in the sensitivity function obtained from observations of standard stars.

Table 4: H II regions in NGC 1705.

ΗII		
Region	MMT85	MFDC92
(1)	(2)	(3)
A1		
A2	В	H2
A3		H1
A4		
B1	\mathbf{C}	H3
B2		• • •
В3		
$\mathrm{B4^{a}}$		
B5		• • •
${ m B6^{b}}$	D	H4
B7		
B8		
C1		H5
$\mathrm{C2}^{\mathrm{c}}$		
$\mathrm{C3}^{\mathrm{b}}$	D	H4
C4		
$\mathrm{C5}^{\mathrm{d}}$	A	N
С6 е		

^aThe pixels defining the extraction aperture for B4 encompass the H II regions B3 and B5.

^bB6 and C3 are the same H II region.

^cThe pixels defining the extraction aperture for C2 encompass the H II regions C1 and C3.

^dSuper star cluster (SSC), or NGC 1705-1. The spectrum of the SSC shown in Fig. 6 exhibits weak [O III] $\lambda\lambda$ 4959,5007 and Hα emission, also seen previously by Melnick et al. (1985). This spectrum is not included in the present analysis.

 $[^]e$ The pixels defining the extraction aperture for C6 encompasses light from H II regions A3 and A4.

Note. — Col. (1): H II regions identified in Figs. 2 to 4. Cols. (2) and (3): Identifications with previous work – MMT85: Melnick et al. (1985, their Fig. 2), MFDC92: Meurer et al. (1992, their Table 5 and Fig. 12).

Table 5a: Line ratios and properties for H II regions A1 to A4 inclusive.

$\begin{array}{c c} A3 & & I \\ \hline 4 & 254 \pm 12 \\ 4 & 48.6 \pm 2.4 \\ 24.3 \pm 3.2 \\ 0 & 28.3 \pm 1.5 \end{array}$	
48.6 ± 2.4 24.3 ± 3.2	
24.3 ± 3.2	
$0 28.3 \pm 1.5$	
$3 2.04 \pm 0.76$	
26.1 ± 1.4	
49.8 ± 1.8	
4.1 ± 1.2	
3.60 ± 0.57	
100.0 ± 3.3	
147 ± 11	
425 ± 14	
$1 10.3 \pm 0.77$	
$7 291 \pm 15$	
9.3 ± 6.8	
4.2 ± 1.1	
33.8 ± 2.1	
3.46 ± 0.59	
7.3 ± 1.1	
$0.12) \times 10^{-15}$	
80.1 ± 4.5	
72 ± 0.089	
21 ± 0.060	
+0.47	
2.1 ± 1.1	
0 1 2 7 (C C C C C C C C C C C C C C C C C C	

^aBlended with [Ne III] λ 3968.

Note. — Emission lines are listed in Å. F is the observed flux ratio with respect to H β . I is the corrected intensity ratio, corrected for the adopted reddening listed, and for underlying Balmer absorption. The uncertainties in the observed line ratios account for the uncertainties in the fits to the line profiles, the surrounding continua, and the relative uncertainty in the sensitivity function listed in Table 3. Flux uncertainties in the H β reference line are not included. Uncertainties in the corrected line ratios account for uncertainties in the specified line and in the H β reference line. The reddening function, $f(\lambda)$, from Equation (2) is given. Also listed are the observed H β flux; the equivalent width of H β in emission, EW_e(H β); derived values of the reddenings from SNAP using Equation (1). Where [O III] λ 4363 is measured, simultaneous solutions for the logarithmic reddening, $c(H\beta)$, from Equation (2) and the equivalent width of the underlying Balmer absorption, EW_{abs}, are listed. The adopted value of the extinction in V, A_V , is listed. Where [O III] λ 4363 is not measured, the equivalent width of the underlying Balmer absorption was set to 2 Å.

Table 5b: Line ratios and properties for H II regions B1 to B8 inclusive.

	B1			P	32	B3		
Wavelength (Å)	$f(\lambda)$	F	I	F	1 I	F	I	
[O II] 3727	+0.325	414 ± 14	400 ± 51	462 ± 13	475 ± 60	300.7 ± 6.3	274 ± 7.1	
[Ne III] 3869	+0.294	48.6 ± 9.4	47 ± 13	65.7 ± 6.5	66 ± 12	67.0 ± 2.9	61.0 ± 2.8	
$H\epsilon + He I 3970$	+0.269					9.9 ± 2.2	22.2 ± 2.0	
$H\delta$ 4101	+0.232					14.4 ± 2.0	25.6 ± 1.8	
$H\gamma$ 4340	+0.158	62.2 ± 6.7	64 ± 13	40.9 ± 3.7	50 ± 10	39.5 ± 2.1	46.8 ± 1.9	
[O III] 4363	+0.151	• • •				6.1 ± 1.6	5.6 ± 1.5	
He I 4471 He II 4686	+0.116 +0.050					3.94 ± 0.94 5.42 ± 0.63	3.59 ± 0.86 4.93 ± 0.57	
Hβ 4861	0.000	100.0 ± 6.7	100.0 ± 7.9	100.0 ± 6.7	100.0 ± 8.2	100.0 ± 4.5	100.0 ± 4.1	
[O III] 4959	-0.026	106.5 ± 8.8	103 ± 17	147 ± 12	132 ± 22	183 ± 14	167 ± 13	
[O III] 5007	-0.038	326 ± 11	315 ± 40	412 ± 15	367 ± 49	534 ± 18	486 ± 16	
He I 5876	-0.204					8.59 ± 0.94	7.82 ± 0.86	
$H\alpha$ 6563	-0.299	292 ± 10	285 ± 37	340 ± 11	286 ± 38	302.5 ± 9.1	281.3 ± 9.1	
[N II] 6583	-0.302	4.1 ± 8.6	3.9 ± 8.7	14.9 ± 4.2	12.2 ± 4.5	10.8 ± 1.8	9.8 ± 1.6	
He I 6678	-0.314					3.1 ± 1.1	2.8 ± 1.0	
[S II] 6716, 6731	-0.320	50.9 ± 6.4	49 ± 10	20.2 ± 3.6	16.4 ± 4.4	40.8 ± 3.0	37.1 ± 2.8	
[Ar III] 7136	-0.375					9.8 ± 1.4	9.2 ± 1.9	
$F(H\beta)$ (ergs s ⁻¹	cm^{-2})	(9.92 ± 0.6)	6) $\times 10^{-16}$	(1.444 ± 0.0)	$96) \times 10^{-15}$	(5.30 ± 0.2)	$4) \times 10^{-15}$	
$\dot{\mathrm{EW}}_{\mathrm{e}}(\mathrm{H}\beta)$ ($\pm^{'}$ 5.5		$\pm \hat{1}.3$	35.5		
Derived $E(B - V)$			± 0.130		± 0.132		± 0.107	
$c(H\beta)$		-				-0.009		
Adopted A_V)	0.		(
$\mathrm{EW}_{\mathrm{abs}}$ (A	1)	2	2	2	2	3.7 =	± 1.2	
	4(3)		4		55	В		
Wavelength (Å)	$f(\lambda)$	F 245 4 7.2	I 212 8.0	F 200 0 1 0 0	1 240 26	F	I 426 10	
[O II] 3727	+0.325	345.4 ± 7.2	312 ± 8.0	398.8 ± 8.8	349 ± 36 90 ± 13	484.7 ± 9.9	436 ± 19	
[Ne III] 3869 Ηγ 4340	+0.294 +0.158	80.4 ± 4.2 37.6 ± 2.1	72.7 ± 3.8 45.8 ± 1.9	103.2 ± 7.1 33.7 ± 2.7	45.2 ± 8.1	77.6 ± 5.2 39.9 ± 2.0	69.9 ± 5.3 46.9 ± 2.0	
[O III] 4363	+0.150 +0.151	5.3 ± 1.6	4.8 ± 1.5	33.7 ± 2.7	45.2 ± 6.1	6.3 ± 1.6	5.7 ± 1.5	
He I 4471	+0.116	2.68 ± 0.92	2.42 ± 0.83			0.0 ± 1.0		
He II 4686	+0.050	3.96 ± 0.57	3.58 ± 0.52					
Hβ 4861	0.000	100.0 ± 4.5	100.0 ± 4.1	100.0 ± 4.5	100.0 ± 6.2	100.0 ± 4.2	100.0 ± 3.8	
[O III] 4959	-0.026	189 ± 14	171 ± 13	193 ± 15	169 ± 25	158 ± 14	145 ± 13	
[O III] 5007	-0.038	546 ± 19	494 ± 57	558 ± 19	487 ± 54	466 ± 19	427 ± 18	
He I 5876	-0.204	8.24 ± 0.98	7.45 ± 0.89	7.4 ± 1.3	6.5 ± 1.6	10.8 ± 1.3	10.0 ± 1.2	
$H\alpha 6563$	-0.299	309.3 ± 9.4	286.0 ± 9.4	316 ± 10	284 ± 31	300 ± 10	284 ± 13	
[N II] 6583	-0.302	7.6 ± 1.5	6.9 ± 1.4	10.8 ± 3.4	9.5 ± 3.5	16.0 ± 3.6	14.8 ± 3.4	
[S II] 6716, 6731	-0.320	39.6 ± 3.4	35.8 ± 2.2	44.2 ± 3.1	37.8 ± 7.8	49.9 ± 5.9	46.7 ± 5.7	
[Ar III] 7136	-0.375	10.6 ± 1.5	9.6 ± 1.9	10.2 ± 1.6	8.9 ± 2.0	11.9 ± 1.7	11.0 ± 2.2	
$F(H\beta)$ (ergs s ⁻¹	cm^{-2}	(8.84 ± 0.4)	$0) \times 10^{-15}$	(2.85 ± 0.1)	$3) \times 10^{-15}$	(4.27 ± 0.1)	$8) \times 10^{-15}$	
$\mathrm{EW_{e}}(\mathrm{H}\beta)$ ((Å)	21.8	$\pm \ 1.0$	13.9	± 0.64	24.5 ± 1.1		
Derived $E(B - V)$	$^{\prime})~(\mathrm{mag})$		± 0.109		± 0.112	-0.013 ± 0.108		
$c(H\beta)$	(\		010			-0.		
Adopted A _V			.02)	$0 \\ 2.3$		
EW _{abs} (A	1)		.6		2	2	.3	
Wavelength (Å)	$f(\lambda)$	F	I	F	88 I			
[O II] 3727	+0.325	271.4 ± 7.3	264 ± 25	490 ± 20	513 ± 86			
[Ne III] 3869	+0.294	60.9 ± 6.5	59.3 ± 9.8					
$H\epsilon + He I 3970$	+0.269	27.8 ± 4.8	30.6 ± 7.7					
$H\delta$ 4101	+0.232	28.3 ± 3.0	31.1 ± 5.5	35.0 ± 7.1	37 ± 12			
$H\gamma 4340$	+0.158	50.4 ± 2.6	52.1 ± 6.1	34.1 ± 5.4	36 ± 10			
H $β$ 4861	0.000	100.0 ± 3.8	100.0 ± 5.3	100 ± 10	100 ± 12			
[O III] 4959	-0.026	116.5 ± 8.7	113 ± 15	60.1 ± 7.4	59 ± 14			
[O III] 5007	-0.038	349 ± 11	340 ± 34	207.6 ± 9.7	204 ± 35			
He I 5876	-0.204	7.8 ± 1.7	7.6 ± 2.1	200 12				
Hα 6563	-0.299	288.5 ± 9.2	283 ± 28	302 ± 13	286 ± 49			
[S II] 6716, 6731	-0.320	33.6 ± 3.6	32.7 ± 5.4					
$F(H\beta)$ (ergs s ⁻¹		(3.31 ± 0.1)		(6.83 ± 0.7)				
$EW_{e}(H\beta)$ (± 4.2		± 55			
Derived $E(B - V)$	(mag)		± 0.102		± 0.172			
$c({ m H}eta)$ Adopted A_V	(mag)))		.13			
			2		2			
EW _{abs} (A)			-					

Table 5c: Line ratios and properties for H II regions C1, C2, C3, C4, and C6.

			1-1		10		10	
Worder of (8)	r(X)		;1 ,		⁷		13	
Wavelength (Å)	$f(\lambda)$	<i>F</i>	<i>I</i>	267 0 ± 7 0	<i>I</i>	425 9 ± 9 6	1 409 ± 20	
[O II] 3727	+0.325	332.5 ± 7.1	401 ± 38	367.0 ± 7.9	402 ± 38	425.8 ± 8.6	408 ± 39	
[Ne III] 3869	+0.294	27.4 ± 1.4	31.8 ± 3.7	41.3 ± 1.7	44.2 ± 4.8	67.7 ± 3.2	64.7 ± 7.4	
H8 + He I 3889	+0.289	11.0 ± 1.2	18.5 ± 3.9	9.8 ± 1.4	18.0 ± 4.7	8.6 ± 2.5	17.7 ± 9.5	
$H\epsilon + He I 3970$	+0.269	16.6 ± 1.3	24.3 ± 3.9	13.0 ± 1.4	21.1 ± 4.4	12.0 ± 2.4	21.0 ± 7.6	
$H\delta$ 4101	+0.232	17.6 ± 1.4	24.5 ± 3.8	15.9 ± 1.3	23.3 ± 3.9	15.6 ± 2.1	23.8 ± 5.9	
$H\gamma 4340$	+0.158	43.0 ± 1.3	49.3 ± 5.1	42.2 ± 1.5	48.0 ± 5.2	42.6 ± 2.6	47.6 ± 6.5	
[O III] 4363	+0.151	< 3.50	< 3.67	< 5.64	< 5.67	< 10.4	< 9.89	
He I 4471	+0.116	3.86 ± 0.71	3.97 ± 0.96	2.97 ± 0.65	2.94 ± 0.82	100.0 4.1	100.0 5.0	
$H\beta$ 4861	0.000	100.0 ± 4.0	100.0 ± 5.4	100.0 ± 3.9	100.0 ± 5.4	100.0 ± 4.1	100.0 ± 5.6	
[O III] 4959	-0.026	113.8 ± 7.3	109 ± 14	132.1 ± 8.7	126 ± 16	167 ± 12	157 ± 21	
[O III] 5007	-0.038	334.7 ± 9.5	319 ± 31	379 ± 11	359 ± 36	467 ± 15	439 ± 45	
He I 5876	-0.204	8.65 ± 0.81	7.5 ± 1.2	6.52 ± 0.87	5.8 ± 1.1	7.4 ± 1.3	6.9 ± 1.6	
$H\alpha$ 6563	-0.299	342.9 ± 7.5	286 ± 27	326.1 ± 8.2	286 ± 28	304.5 ± 9.8	286 ± 30	
[N II] 6583	-0.302	11.7 ± 4.0	9.7 ± 3.9	17.7 ± 5.4	15.4 ± 5.6	13.2 ± 3.2	12.2 ± 3.6	
He I 6678	-0.314	•••	•••	•••	•••	5.8 ± 2.0	5.4 ± 2.2	
[S II] 6716, 6731	-0.320	44.9 ± 2.6	43.2 ± 5.3	49.9 ± 3.0	43.2 ± 5.3	49.7 ± 2.7	46.0 ± 5.5	
$F(H\beta)$ (ergs s ⁻¹	cm^{-2})	(4.90 ± 0.2)	$0) \times 10^{-15}$	(8.48 ± 0.3)	$(3) \times 10^{-15}$	$(2.55 \pm 0.10) \times 10^{-15}$		
$\mathrm{EW_{e}}(\mathrm{H}\beta)$ (Å)	64.5	$\pm \ 3.8$	45.3	± 2.2	31.6 ± 1.5		
Derived $E(B - V)$	(mag)	+0.159	$+0.159 \pm 0.097$		± 0.098	$+0.014 \pm 0.105$		
$c(H\beta)$		• • •		•	• •	•••		
Adopted A_V ((mag)	+0.49		+0	.30	+0.04		
EW_{abs} (Å	.)	2		4	2	2	2	
		C	4	C	C6			
Wavelength (Å)	$f(\lambda)$	F	I	F	I			
[O II] 3727	+0.325	354.6 ± 9.1	352 ± 56	310.0 ± 5.9	301.8 ± 7.3			
[Ne III] 3869	+0.294	91.3 ± 7.8	89 ± 18	49.1 ± 1.5	47.8 ± 1.6			
H8 + He I 3889	+0.289	• • •	• • •	18.9 ± 1.3	23.4 ± 1.3			
$H\epsilon + He I 3970$	+0.269			25.3 ± 1.3	29.4 ± 1.3			
${ m H}\delta$ 4101	+0.232	• • •	• • •	20.3 ± 1.5	24.1 ± 1.5			
$H\gamma 4340$	+0.158	23.2 ± 2.9	38 ± 12	47.4 ± 1.5	49.6 ± 1.5			
[O III] 4363	+0.151	• • •	• • •	3.4 ± 1.2	3.3 ± 1.2			
$_{\mathrm{H}\beta}$ 4861	0.000	100.0 ± 9.6	100 ± 12	100.0 ± 3.7	100.0 ± 3.6			
[O III] 4959	-0.026	188 ± 10	163 ± 29	141 ± 10	137.3 ± 9.7			
[O III] 5007	-0.038	536 ± 13	464 ± 73	404 ± 14	393 ± 14			
He I 5876	-0.204			7.87 ± 0.80	7.66 ± 0.78			
$H\alpha 6563$	-0.299	350 ± 10	286 ± 47	285.7 ± 7.9	279.7 ± 8.6			
[N II] 6583	-0.302	2.0 ± 8.9	1.6 ± 7.4	6.4 ± 6.7	6.2 ± 6.5			
[S II] 6716, 6731	-0.320	48.5 ± 4.3	38.5 ± 8.1	37.5 ± 1.9	36.5 ± 1.9			
[Ar III] 7136	-0.375			6.8 ± 1.0	6.6 ± 1.3			
$F(H\beta)$ (ergs s ⁻¹	cm^{-2}	(2.38 ± 0.2)	$3) \times 10^{-15}$	$(1.040 \pm 0.0$	$(38) \times 10^{-14}$			
$\mathrm{EW_{e}}(\mathrm{H}\beta)$ (ergs s	,	*	± 1.4	•	± 4.2			
Derived $E(B-V)$			± 0.164		± 0.098			
$c(H\beta)$, (11145)				± 0.066			
Adopted A_V ((mag)		.28		0.000			
			2		± 1.4			
EW _{abs} (Å)		-	-	2.0	L 1.4			

Table 6a. Ionic and total abundances.

Property	A1	A2	A3	A4	B1	B2	В3	B4	B5
$T_e({\rm O}^{+2}) \; ({\rm K})$	< 20300		11400 ± 1200				12100 ± 1200	11400 ± 1300	
$T_e(\mathrm{O^+})$ (K)	< 17200		11000 ± 1200				11500 ± 1200	11000 ± 1200	
$O^{+}/H \ (\times 10^{5})$	> 2.1		6.5 ± 2.7				5.8 ± 2.3	7.9 ± 3.5	
$O^{+2}/H (\times 10^5)$	> 1.6		9.8 ± 3.0				9.3 ± 2.7	11.3 ± 3.7	
$O/H (\times 10^5)$	> 3.7		16.2 ± 4.0				15.1 ± 3.5	19.2 ± 5.1	
$12 + \log(\mathrm{O/H})$	> 7.57		$8.21 \pm 0.10 \binom{+0.11}{-0.16}$				$8.18 \pm 0.09 \binom{+0.11}{-0.14}$	$8.28 \pm 0.10 \binom{+0.12}{-0.16}$	
$12 + \log({\rm O/H}) {\rm M91^{a}}$	8.21	8.33	8.15	8.11	8.25		8.25	8.31	8.35
$12 + \log({\rm O/H}) \ {\rm P00^{b}}$	8.14	8.11	7.96	7.93	8.18	8.29	8.02	8.08	8.13
$Ar^{+2}/H (\times 10^7)$			5.1 ± 2.2				5.8 ± 2.9	6.8 ± 3.5	
ICF(Ar)			1.46				1.47	1.46	
$Ar/H (\times 10^7)$			7.5 ± 3.2				8.5 ± 4.2	9.8 ± 5.1	
$\log(Ar/O)$			-2.34 ± 0.23				-2.26 ± 0.27	-2.29 ± 0.29	
$N^{+}/O^{+} (\times 10^{2})$			2.2 ± 1.6				2.34 ± 0.42	1.34 ± 0.28	
$\log(N/O)$			-1.65 ± 0.24				-1.63 ± 0.07	-1.87 ± 0.08	
Ne^{+2}/O^{+2}			0.346 ± 0.051				0.356 ± 0.058	0.429 ± 0.078	
$\log({ m Ne/O})$			-0.460 ± 0.063				-0.448 ± 0.070	-0.367 ± 0.078	

^aMcGaugh (1991) bright-line calibration.

Note. — Direct oxygen abundances are shown with two uncertainties. The first uncertainty is the formal uncertainty in the derivation. In parentheses is the range of possible values, expressed by the maximum and minimum values of the oxygen abundance.

^bPilyugin (2000) bright-line calibration.

-34 -

Table 6b. Ionic and total abundances (continued).

Property	В6	В7	В8	C1	C2	С3	C4	С6
$T_e(\mathrm{O}^{+2})$ (K)	12900 ± 1400			< 12100	< 13700	< 16100		10900 ± 1400
$T_e(\mathrm{O}^+)$ (K)	12000 ± 1400			< 11500	< 12600	< 14200		10600 ± 1400
${ m O^{+}/H}~(\times 10^{5})$	7.8 ± 3.0			> 8.4	> 6.0	> 4.0		8.9 ± 4.7
${ m O}^{+2}/{ m H}~(imes 10^5)$	6.8 ± 1.9			> 6.0	> 4.8	> 4.0		10.7 ± 4.2
$O/H \ (\times 10^5)$	14.6 ± 3.6			> 14	> 11	> 8.0		19.6 ± 6.3
$12 + \log(\mathrm{O/H})$	$8.17 \pm 0.10 \binom{+0.11}{-0.14}$			> 8.16	> 8.04	> 7.90		$8.29 \pm 0.12 \left(^{+0.14}_{-0.20}\right)$
$12+\log({\rm O/H})$ M91 $^{\rm a}$		8.08	8.31	8.26	8.30		8.33	8.21
$12 + \log(\mathrm{O/H})$ P00 $^{\mathrm{b}}$	8.23	7.94	8.46	8.18	8.18	8.20	8.12	8.03
$Ar^{+2}/H (\times 10^7)$	6.2 ± 3.0							5.1 ± 2.7
ICF(Ar)	1.49							1.45
$Ar/H (\times 10^7)$	9.3 ± 4.4							7.3 ± 3.9
$\log(Ar/O)$	-2.19 ± 0.26							-2.41 ± 0.32
$N^{+}/O^{+} (\times 10^{2})$	2.37 ± 0.57							
$\log(N/O)$	-1.63 ± 0.09							
Ne^{+2}/O^{+2}	0.452 ± 0.083							0.359 ± 0.063
$\log({ m Ne/O})$	-0.345 ± 0.079			• • •	• • •	• • •		-0.444 ± 0.075

^aMcGaugh (1991) bright-line calibration.

Note. — See Table 6a for comments.

^bPilyugin (2000) bright-line calibration.

Table 7. Neutral and nebular gas phase abundances.

Property (dex)	НІ	H II (mean)
12+log(O/H)	7.43 ± 0.3	8.21 ± 0.05
$12 + \log(N/H)$	5.73 ± 0.3	6.46 ± 0.08
$\log(\mathrm{N/O})$	-1.70 ± 0.4	-1.75 ± 0.06
$12 + \log(Ar/H)$	5.26 ± 0.3	5.91 ± 0.10
$\log({\rm Ar/O})$	-2.17 ± 0.4	-2.31 ± 0.11

Note. — Neutral gas (H I) phase abundances are taken from Heckman et al. (2001); they assign 0.3 dex uncertainties for the total abundances, and we have derived approximate 0.4 dex uncertainties for the abundance ratios. Nebular gas (H II) phase abundances are taken from the present work.

This figure "fig01a.jpg" is available in "jpg" format from:

http://arXiv.org/ps/astro-ph/0406571v2

This figure "fig01b.jpg" is available in "jpg" format from:

This figure "fig02a.jpg" is available in "jpg" format from:

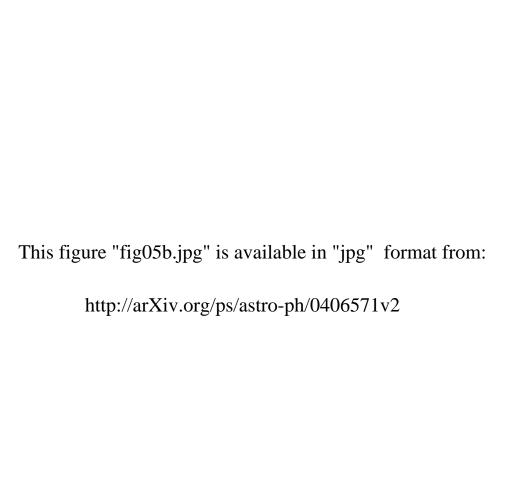
This figure "fig02b.jpg" is available in "jpg" format from:

This figure "fig03a.jpg" is available in "jpg" format from:

This figure "fig03b.jpg" is available in "jpg" format from:

This figure "fig04.jpg" is available in "jpg" format from:

This figure "fig05a.jpg" is available in "jpg" format from: http://arXiv.org/ps/astro-ph/0406571v2



This figure "fig05c.jpg" is available in "jpg" format from: http://arXiv.org/ps/astro-ph/0406571v2

This figure "fig05d.jpg" is available in "jpg" format from:

This figure "fig06.jpg" is available in "jpg" format from:

This figure "fig07.jpg" is available in "jpg" format from:

This figure "fig08.jpg" is available in "jpg" format from:

This figure "fig09.jpg" is available in "jpg" format from:

This figure "fig10.jpg" is available in "jpg" format from:

This figure "fig11.jpg" is available in "jpg" format from: